Universitat Autònoma de Barcelona

Multiplex Optical Detection System for Prosthetic Joint Infection Diagnosis

Bernat Mir de Simón

Universitat Autònoma
de Barcelona

Programa de Doctorado en Cirugía y Ciencias Morfológicas
Departamento de Cirugía
Facultad de Medicina

Multiplex Optical Detection System for Prosthetic Joint Infection Diagnosis

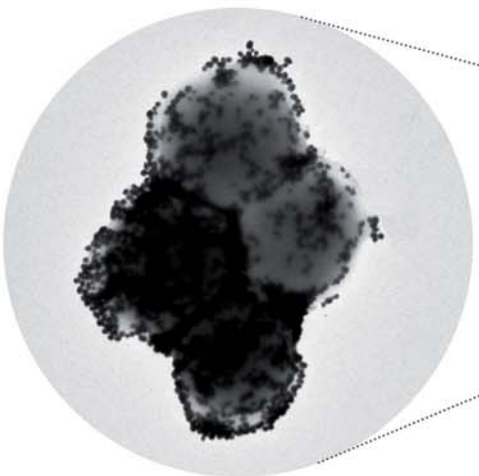

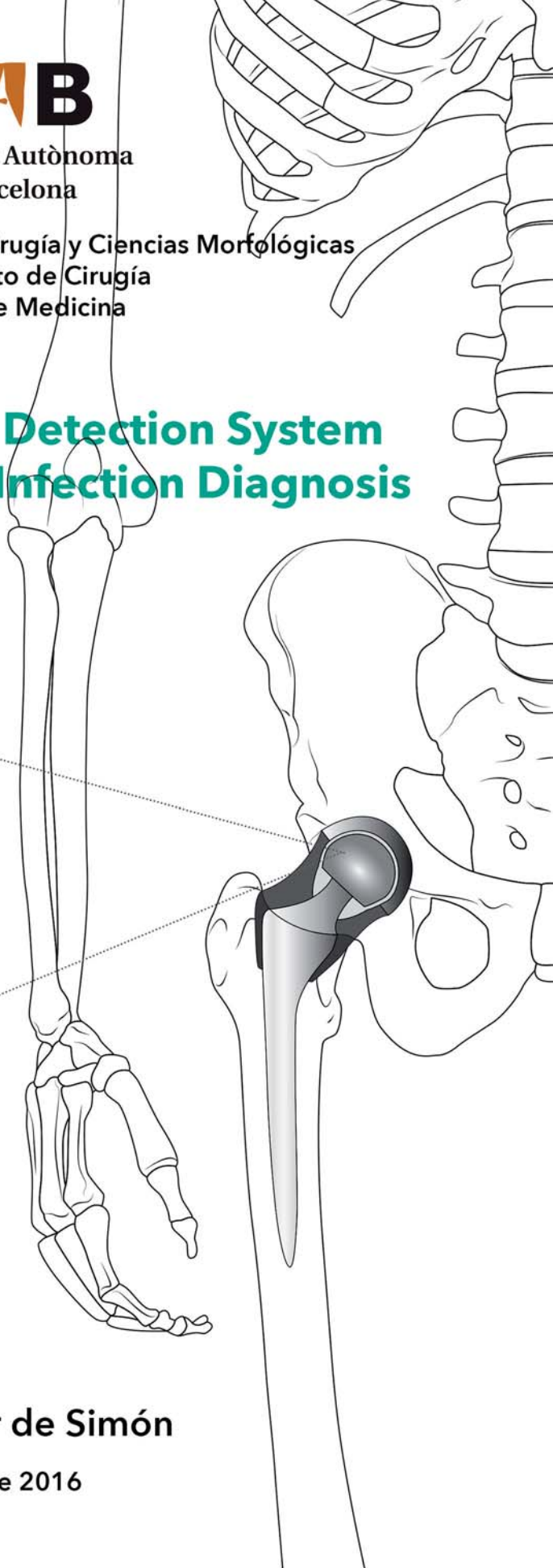

Bernat Mir de Simón

Octubre 2016

Universitat Autònoma de Barcelona

Programa de Doctorado en Cirugía y Ciencias Morfológicas

Departamento de Cirugía

Facultad de Medicina

Multiplex Optical Detection System for Prosthetic Joint Infection Diagnosis

Memoria de tesis doctoral presentada por **Bernat Mir de Simón** para optar al grado de doctor por la Universidad Autónoma de Barcelona.

Barcelona, 2016

Doctorando Bernat Mir de Simón

Director y tutor Francisco Javier Mir Bulló

Codirector Ramón Álvarez Puebla

Barcelona, 2016

El Dr. Francisco Javier Mir Bulló, Profesor titular de Cirugía Ortopédica y Traumatología de la Facultad de Medicina de la Universidad Autónoma de Barcelona, jefe de la Unidad de Extremidad Superior del Hospital Universitario de la Vall d'Hebron y jefe de la Unidad de Mano y Microcirugía del Hospital Universitario Quiron Dexeus.

CERTIFICA:

Que Don **Bernat Mir de Simón** ha realizado bajo la dirección de los abajo firmantes el trabajo de investigación correspondiente a la tesis doctoral:

MULTIPLEX OPTICAL DETECTION SYSTEM FOR PROSTHETIC JOINT INFECTION DIAGNOSIS

Revisado el presente trabajo, estimo que corresponde fielmente a los resultados obtenidos y quedo conforme con su presentación para ser juzgado por el tribunal que sea designado para su lectura.

Prof. Francisco Javier Mir Bulló

Barcelona, 2016

Directores de la tesis:

Dr. Francisco Javier Mir Bulló

Departamento de Cirugía

H. U., Vall d'Hebron, Barcelona

Dr. Ramón Álvarez Puebla

Departamento de Química Física e Inorgánica

Universitat Rovira i Virgili, Tarragona

Agradecimientos

Cuando finalicé la licenciatura en Ingeniería Química quien hubiera dicho que acabaría haciendo una tesis en medicina. Después de estar trabajando durante 3 años en el sector energético, una inquietud creciente en mí me hizo realizar un cambio drástico en mi vida. Gracias a mi padre, me di cuenta que esa inquietud residía en el mundo médico. Los cambios radicales nunca son fáciles y solo son posibles si la gente que te rodea, te apoya y te ayuda a resolver la infinidad de dudas que surgen. Por ello, me gustaría agradecer a todas las personas que han hecho de esta tesis una realidad.

En primer lugar quisiera mostrar mi gratitud a mi director de tesis por haberme dado la oportunidad de cumplir un sueño. Al Prof. Xavier Mir Bulló, por su apoyo incondicional, por hacer aflorar la pasión médica en mi ser, por infundirme un valor inquebrantable y por ser un gran padre.

Al Dr. Nicolás Pazos Pérez, por haberme enseñado desde el minuto 0 y de la forma más clara y amena posible gran parte de los conocimientos de síntesis y caracterización de nanopartículas que a día de hoy poseo. Tengo que agradecerle también la confianza depositada en mí y por tratarme con el equilibrio perfecto entre pupilo y amigo.

A las Dras. Elena Pazos Chantrero y Sara Gómez de Pedro, por sus valiosos y sabios consejos, por poder discutir con ellas infinidad de problemas y siempre encontrar la solución, por aguantarme y hacerme reír y por ser unas grandes amigas.

Al Dr. Luca Guerrini, por hacerme ver la ciencia de forma estricta y metódica y a los Dres. Alexey Shavel, Hainan Xie y Moritz Nazarenus, por sus correcciones y sugerencias durante las reuniones de grupo.

Al equipo del Dr. Lluís Carrera del Hospital Universitario de la Vall d'Hebron, por su apoyo y por sus enseñanzas sobre la infección protésica articular.

Al Prof. Javier García de Abajo, por las simulaciones electromagnéticas y de SERS realizadas las cuales han permitido el correcto desarrollo de la investigación.

Al Prof. Victor Puntes y a la Dra. Neus Bastús por la síntesis controlada de nanopartículas de oro de diferentes tamaños.

Al equipo del Dr. Álex Soriano del Hospital Clínic de Barcelona, por su aporte y asesoramiento en el diagnóstico y patogénesis de infecciones agudas.

A mis compañeros, Patri por ser una buena confidente, Judit por sus críticas constructivas (o no tanto), Manu por ayudarme con todos los conocimientos de "bio", Alicia por haberme dado ganas de seguir adelante, Arnau por haber compartido innumerables horas de síntesis, Xiatong por ser tú, Ana por ser tan sincera y Carme por tus "bichos". Además, quisiera agradecer a todos ellos su amistad, cariño y por haberme hecho reír en multitud de ocasiones.

A Juan Sagalés Mañas, por haberme brindado una de las mejores oportunidades a nivel profesional de mi vida.

Al equipo de microscopia de la universidad Rovira i Virgili (especialmente a la Dra. Rita Marimón), por sus enseñanzas en microscopia electrónica de transmisión y microscopia electrónica de barrido ambiental.

A mi madre y mi tía, por haberme ayudado tanto siempre y por hacer que me esfuerce cada día más.

Finalmente tengo que agradecer a Bo Min, por ser mi alma gemela y mi muleta, por darme cada día las fuerzas necesarias para creer en mi mismo y por hacer que siempre cumpla mis objetivos. Sin ella esto no habría sido posible.

Table of contents

Acronyms (by alphabetical order)

1NT: 1-NAPHTALENETHIOL

2356TFBT: 2,3,5,6-TETRAFLUORO BENZENETHIOL

2FTP: 2-FLUOROTHIOPHENOL

2MBA: 2-MERCAPTOBENZOIC ACID

2NT: 2-NAPHTALENETHIOL

2PET: 2-PHENYLETHANETHIOL

2TFMBT: 2-(TRIFLUOROMETHYL) BENZENETHIOL

35BTFMBT: 3,5-BIS(TRIFLUOROMETHYL) BENZENETHIOL

3FTP: 3-FLUOROTHIOPHENOL

4ATP: 4-AMINOTHIOPHENOL

4FTP: 4-FLUOROTHIOPHENOL

4MBA: 4-MERCAPTOBENZOIC ACID

4MP: 4-MERCAPTOPHENOL

4NBT: 4-NITROBENZENETHIOL

AA: L-ASCORBIC ACID

Ab: ANTIBODY

Ag: SILVER

$AgNO_3$: SILVER NITRATE

Apt: APTAMER

ATT: 5-AMINO-1,3,4-THIADIAZOLE-2-THIOL

Au: GOLD

BEM: BOUNDARY-ELEMENT METHOD

BPDT: BIPHENYL-4-4'-DITHIOL

BPT: BIPHENYL-4-THIOL

BT: BENZENETHIOL

$C_6H_5Na_3O_7 \cdot 2H_2O$: TRISODIUM CITRATE

CE: CHEMICAL ENHANCEMENT

CFU: COLONY FORMING UNIT

CRP: C-REACTIVE PROTEIN

CT: CHARGE TRANSFER

CTAB: CETYL-TRIMETHYLAMMONIUM BROMIDE

CV: CRYSTAL VIOLET

DAIR: DEBRIDEMENT, ANTIBIOTICS, IRRIGATION AND RETENTION OF THE PROSTHESIS.

DCBT: 3,4-DICHLOROBENZENETHIOL

DLVO: VERWEY AND OVERBEEK DEVELOPED THEORY

DMF: N,N-DIMEMETHYLFORMAMIDE

EBJIS: EUROPEAN BONE AND JOINT INFECTION SOCIETY

EDC: 1-ETHYL-3-(3-DIMETHYLAMINOPROPYL) CARBODIIMIDE HYDROCHLORIDE)

EF: ENHANCEMENT FACTOR

ELISA: ENZYME-LINKED IMMUNE SORBENT ASSAY

EM: ELECTROMAGNETIC MECHANISM

EPS: EXTRACELLULAR POLYMERIC SUBSTANCE

ESEM: ENVIRONMENTAL ELECTRON MICROSCOPY

ESR: ERYTHROCYTE SEDIMENTATION RATE

EtOH: ETHANOL

FIA: FLUORESCENCE IMMUNE ASSAY

GNS: GOLD NANOSTARS

$HAuCl_4$: GOLD(III) CHLORIDE TRIHYDRATE

HOMO: HIGHEST OCCUPIED MOLECULAR ORBITAL

HPHTT: 1-(4-HYDROXYPHENYL)-1H-TETRAZOLE-5-THIOL

HS-PEG-COOH: *O*-(2-MERCAPTOETHYL)-*O'*-(2-CARBOXYETHYL) HEPTAETHYLENE GLYCOL

HS-PEG$_{5000}$: *O*-[2-(3-MERCAPTOPROPIONYLAMINO)ETHYL]-*O'*-METHYLPOLYETHYLENE GLYCOL

IR: INFRARED

ISDA: INFECTIOUS DISEASES SOCIETY OF AMERICA

LbL: LAYER BY LAYER

LSPR: LOCALIZED SURFACE PLASMON RESONANCE

LUMO: LOWEST UNOCCUPIED MOLECULAR ORBITAL

MALDI-TOF: MATRIX-ASSISTED LASER DESORPTION/IONIZATION-TIME-OF-FLIGHT

MB: METHYLENE BLUE

MESME: MULTIPLE ELASTIC SCATTERING OF MULTIPOLAR EXPANSIONS

$MgSO_4$: MAGNESIUM SULFATE

MMC: 7-MERCAPTO-4-METHYLCOUMARIN

MMPHTYIMP: 4-(((3-MERCAPTO-5-(2-METHOXYPHENYL)-4H-1,2,4-YL)IMINO) PHENOL

MODS: MICROORGANISM OPTICAL DETECTION SYSTEM

MPHTYIMBA: 4-(((3-MERCAPTO-5-(2-PYRIDINYL)-4H-1,2,4-TRIAZOL-4-YL)IMINO)METHYL) BENZOIC ACID

MPHTYIMBDO: 4-(((3-MERCAPTO-5-(2-PYRIDINYL)-4H-1,2,4-TRIAZOL-4-YL)IMINO)METHYL)-1,2-BENZENEDIOL ACID

MPOT: 5-(4-METHOXYPHENIL)-1,3,4-OXIDAZOLE-2-THIOL

MPy: 4-MERCAPTOPYRIDINE

MS: MASS SPECTROMETRY

MSIS: MUSCULOSKELETAL INFECTION SOCIETY

MUA: 11-MERCAPTOUNDECANOIC ACID

N_2: NITROGEN

$NaBH_4$: SODIUM BOROHYDRIDE

NaCl: SODIUM CHLORIDE

NaOH: SODIUM HYDROXIDE

NAS: NATIONAL ACADEMY OF SCIENCES

NBA: NILE BLUE A

NH_4OH: AMMONIA SOLUTION

NIR: NEAR INFRARED

NIS: NATION-WIDE-IN-PATIENT SAMPLE

NP: NANOPARTICLE

PCR: POLYMERASE CHAIN REACTION

PDMS: POLYDIMETHYLSILOXANE

PEI: POLYETHYLENEIMINE BRANCHED

PJI: PROSTHETIC JOINT INFECTION

PS: POLYSTYRENE BEADS

PSS: POLYSTYRENE SULFONATE

PTFE: POLYTETRAFLUOROETHYLENE

PVP: POLYVINYL PYRROLIDONE

R6G: RHODAMINE 6G

RIA: RADIOIMMUNO ASSAY

RRS: RESONANCE RAMAN SCATTERING

RS: RAMAN SCATTERING

SDS: SODIUM DOCECYL SULFATE

SEM: SCANNING ELECTRON MICROSCOPY

SERRS: SURFACE-ENHANCED RESONANT RAMAN SCATTERING

SERS: SURFACE ENHANCED RAMAN SCATTERING

SiO_2: SILICA

TB: TOLUIDINE BLUE O

TEM: TRANSMISSION ELECTRON MICROSCOPY

TEOS: TETRAETHYL ORTHOSILICATE

TERS: TIP-ENHANCED RAMAN SCATTERING

TPT: 1,1′,4′,1′′-TERPHENYL-4-THIOL

TSA: THIOSALICYLIC ACID

UV-Vis-NIR:

UV: ULTRAVIOLET

Vis: VISIBLE

1 Introduction

Seemingly, trauma, war, diseases and congenital anomalies have accompanied us all through human history. Consequently, amputations and deformity have been dealt with, one way or another, throughout the ages. A prosthesis is an artificial device that replaces a missing or dysfunctional body part and is designed to partially or fully restore its normal functionality.

The evolution of prosthetics has a long and documented history, from its primitive beginnings to its sophisticated present. The Egyptians of the New Empire (16^{th}-11^{th} century BC) were early pioneers of the idea, as shown by the wooden toe in Figure 1. A mummy from this period buried in the Egyptian necropolis near ancient Thebes possessed an artificial big toe consisting of wood and leather. That ancient prosthesis allowed the wearer to walk without crutches. During the 16^{th} century an Italian surgeon noted the existence of an amputee who had an arm that allowed him to remove his hat, open his purse and sign his name.[1] The real improvement in prosthetic design came at the hands of Ambroise Paré, a French surgeon who served kings Henry II, Francis II, Charles IX and Henry III. He is considered one of the fathers of surgery and modern forensic pathology as well as pioneer in surgical techniques and battlefield medicine. Among his inventions was an above-knee device that was a kneeling peg leg and foot prosthesis with a fixed position, adjustable harness, and knee lock control. As the U.S. Civil war dragged on, the number of amputations rose astronomically. It forced the Americans into entering the field of prosthetics. James Hanger, one of the first amputees of the Civil War, developed what he later patented as the "Hanger Limb"[2] from Whittled barrel staves. People such as Hanger helped to transform and advance the prosthetics field with their refinements in mechanisms and materials. At the end of World War II, the National Academy of Sciences (NAS) began to advocate better research and development of prosthetics.

Figure 1. Prosthetic toe from the ancient Egypt. From reference[3].

During the last decades, surgical medicine has evolved considerably and more complicated body parts such as joints can be treated successfully. Nowadays, a surgical procedure called joint replacement is commonly used to remove parts of an arthritic or damaged joint and replaced it with a prosthesis made of plastic, ceramic or metal. These devices are designed to replicate the movement of a normal healthy joint (Figure 2) and can be used in a wide variety of joints such as the wrist, shoulder, elbow, hip and knee. Therefore, joint replacement is considered a life-enhancing procedure for millions of people the world over each year because it provides pain relief, restores function and independence, and improves patient quality of life. In the case of United States, there were 332,000 total hip and 719,000 total knee arthroplasties performed in 2010 and the total number of patients with existing arthroplasties in place continues rising.[4] Interestingly, a larger number of patients in Europe undergo hip arthroplasty than knee arthroplasty.[5,6]

While the majority of joint arthroplasties provide pain-free function, some patients may experience device failure and may require additional surgery at some point during the life of the device. Failure could be aseptic in nature and caused by implant malposition, materials fatigue, a

periprosthetic fracture, a fracture of the prosthetic material itself, loosening at the bone-cement interface or dislocation-in-stability. On the other hand, the device failure could be associated with an infection that involves the joint prosthesis and adjacent tissue, normally called Prosthetic Joint Infection (PJI).

PJI cause significant physical and psychological morbidity on patients and is associated with substantial financial burden on the healthcare system.[7] Using the nation-wide in-patient sample (NIS) data, 2.0% of the total hip arthroplasties and 2.4% of the total knee arthroplasties become infected.[8] However, studies using more precise definitions for PJI, reported that the use of preoperative antimicrobial prophylaxis and a laminar air-flow surgical environment has reduced the risk of intraoperative infection to less than 1.0% after hip and shoulder replacement and to less than 2.0% after knee replacement.[9] In spite of the relatively low incidence of PJI, the financial burden remains enormous. The overall cost to the American health care system to treat PJI was $566 million in 2009 alone.[10] The cost of treating each individual PJI depends in part on the treatment strategy utilized. The cost of a single revision surgery for PJI is higher than the cost of revision for noninfectious reasons (including prolonged procedure duration, increased blood loss, increased use of bone allograft, and increased complications). Moreover, complicated treatments strategies involving multiple individual surgeries further increase the cost.

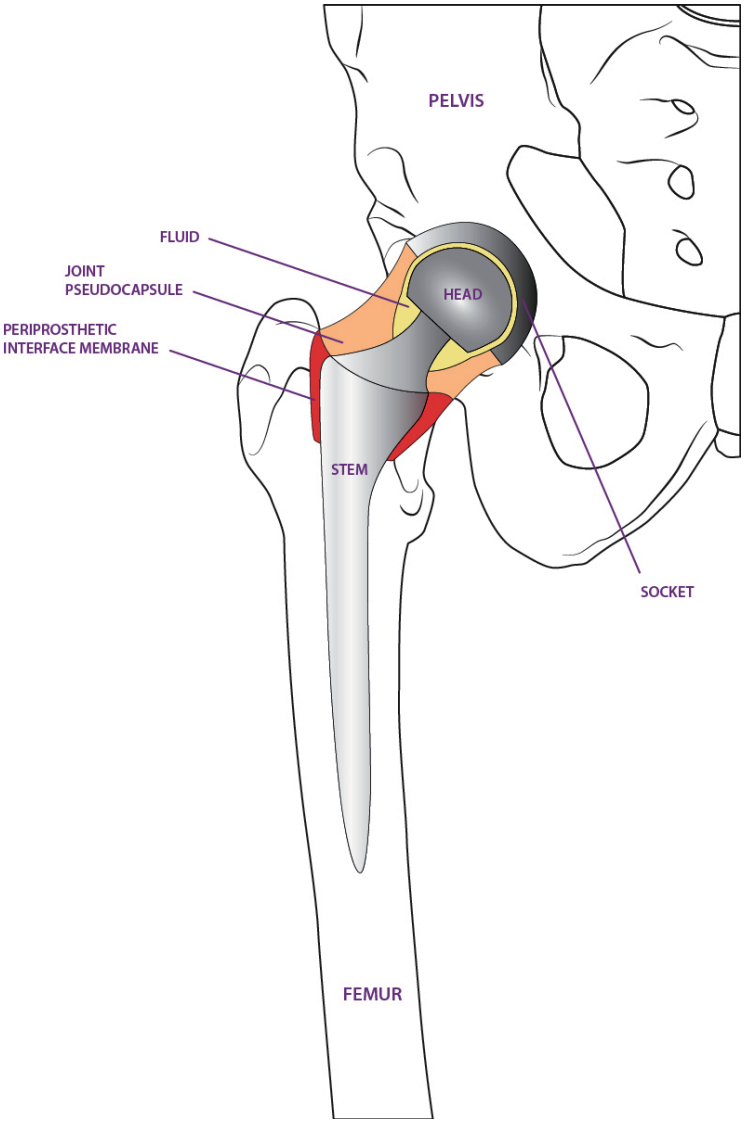

Figure 2. Schematic representation of total hip arthroplasty.

While a small part of joint arthroplasties will become infected, appropriate recognition and management are critical to preserving or restoring adequate function and preventing morbiditiy. Early postoperative and acute hematogenous infections are usually easily diagnosed. However, late chronic infections are challenging to predict and typically caused by microorganisms that grow in biofilms.[11] Within biofilms, microorganisms are enclosed in a polymeric matrix and develop into organized, complex

communities with structural and functional heterogeneity, resembling multicellular organisms.[12] When the microbial density is high, the volume of released cell-to-cell signaling molecules is sufficient to activate genes involved in biofilm production, a phenomenon called quorum sensing.[13] In the biofilm, microbes are protected from antimicrobial agents and host immune responses.

Nowadays, there are no test or findings that are good enough for PJI diagnosis. A complex combination of procedures is required for its diagnosis. They include clinical findings, laboratory results from peripheral blood and synovial fluid, microbiological data, histological evaluation of periprosthetic tissue, intraoperative inspection, and, in some cases, radiographic results. The general approach to PJI diagnosis is 2-fold. First, the question as to whether or not the joint is infected must be answered. Second, if PJI is present, the causative microorganism(s) must be identified and its antimicrobial susceptibility must be determined in most cases. Apart from peripheral blood tests and synovial fluid analysis that relies upon assessing the host response to the infecting pathogen and are only indicative and limited by a low sensitivity,[14] the most valuable diagnostic tools for PJI are actually the intraoperative periprosthetic tissue culture with aerobic and anaerobic blood agar or the fluid culture of the sonicated removed prosthetic components. However, these techniques suffer from intrinsic limitations such as time and sensitivity. Traditionally, the optimal duration of incubation for periprosthetic tissue culture is 4 days for aerobic and 7 days for anaerobic ones. Besides, several studies have recently challenged this dogma and the incubation time was increased to 14 days for some pathogens.[15] On the other hand, microbial culturing may create significant confusion, given the low sensitivity of a single specimen and the difficulty in interpreting potential contamination with low-virulence microorganisms. Standard protocols says that pathogens could be distinguished from contaminants when five tissue specimens were obtained with a sensitivity of 65%.[16,17]

So, it is clear that the development of fast, accurate, and inexpensive diagnostic methods appear as a major goal for alleviating human pain. As

mentioned above, microbial culture remains the most widespread technique for identifying the infectious agent in PJI. Unfortunately, it has low sensitivity and requires 4-14 days to provide a conclusive diagnosis for common infections. As a consequence, a cocktail of broad-spectrum antiobiotics is generally recommended to cover all potential pathogens until a conclusive identification is obtained. Apart from its inherent cost and adverse health effects, this indiscriminate use of antibiotics induces bacterial resistance,[18] a growing problem of modern pharmacopeia.

Surface-enhanced Raman scattering (SERS) spectroscopy[19,20] has been established as a true ultrasensitive, ultra-rapid and universal analytical technique that can provide detection limits even down to the single molecule. A number of direct and label-free applications have been recently developed in fields as diverse as biomedicine, multiplex high-throughput screening, pollutant monitoring or molecular and materials characterization.[21,22] the combination of SERS technique with microfluidics is an emerging application for clinical pathology, especially for immediate point-of-care diagnosis of diseases.[23] This combination started with the use of noble metal nanocolloids as flowing SERS substrates in microfluidic channels.[24] Injecting SERS-active metal colloids into a microfluidic channel not only provides an efficient monitoring platform for lab-on-a-chip systems but also improves SERS technology. Microfluidics emerged at the beginning of the 1980s and it deals with the behavior, precise control and manipulation of fluids that are geometrically constrained to a small, typically sub-millimeter scale.[25] Microfluidic flow could effectively dissipate heat and remove photodamaged analyte molecules from the detection volume under high-power laser excitation.[26] The aim of this thesis is the design of a device based on plasmonic nanoparticles, microfluidic channels and SERS spectroscopy for exhaustive pathogen identification through fast screening for bacterial content of large body-fluid volumes (milliliters), as required by standard medical practice for the analysis of biological samples.[27] This work was oriented toward achieving detection and quantification of bacteria in real time and in a multiplexed manner to improve the diagnosis of PJI.

2 Theoretical background

2.1 Clinical manifestations and Pathogenesis

The clinical manifestations of PJI vary depending upon the virulence of the organism, the mode of initiation of infection, the host immune response, the soft tissue structure surrounding the joint, and the joint involved. Infections associated with prosthetic joints can be classified as early (those that develop less than 3 months after surgery), delayed (3 to 24 months after surgery), or late (more than 24 months after surgery). Early infections typically manifest as an acute onset of joint pain, effusion, erythema and warmth at the implant site, and fever. They are commonly caused by virulent microorganisms like *S. aureus* and *gram-negative bacilli*.[28] During the course of infection, clinically significant cellulitis and the formation of a sinus tract with purulent discharge may occur. Patients with delayed (low-grade) infection usually present with subtle signs and symptoms, such as implant loosening, persistent joint pain, or both. It may be difficult to distinguish from aseptic failure. This infections are usually caused by less virulent microorganisms the like of *coagulase-negative staphylococci* and *P. acnes*. Early and delayed infections are usually acquired during implantation of the prosthesis, whereas late infections are predominantly acquired by hematogenous seeding. The most frequent sources of bacteremia are skin, respiratory tract, dental, and urinary tract infections.[29]

The majority of PJIs take place during the first year of surgery and, normally, the infections are initiated through the introduction of microorganisms at the time of surgery. The prosthesis or the periprosthetic tissue can be contaminated through either direct contact or aerosolized. The first step in the pathogenesis of PJI is the adherence of bacteria to the implant.[30] A significant factor in this process is the low inoculum of microorganisms needed to establish infection in the presence of the prosthetic material. For example, 10^2 colony forming units (CFU) of *S.*

aureus are necessary to establish infection if inoculated at the time of a hip hemiarthroplasty in a rabbit model, compared with 10^4 CFU when no implant is placed.[12] Two distinguishable phases of *reversible* (non-specific) and *irreversible* (specific) attachments occur during bacterial adhesion to the surface of the implant.[30] The reversible attachment works based on the nonspecific physical and chemical characteristics of the bacteria. The biomaterial and surrounding joint fluid also play a role in the reversible adhesion. In contrast, irreversible adhesion depends on more specific structure receptors.[30]

On the other hand, with less incidence, infection from an adjacent site can also initiate PJI by contiguous spread.

2.2 Microbiology

2.2.1 Causative Microorganisms

PJI are usually of bacterial etiology. An infectious arthritis is only rarely caused in this localization by viruses or fungi. The pathogenic mechanisms responsible for articular infections are only well studied for some bacteria, e.g. *Staphylococcus aureus*, while others are only partially understood. The major causative microorganisms of PJI may include:

S. aureus. It is an important pathogen due to its virulence and frequency. In addition to being a leading cause of PJI, it is one of the common causes of serious invasive infections, including nosocomial and health care-associated bloodstream infections that can subsequently lead to PJI.[31,32] Indwelling prosthetic devices, injection drug use, receipt of hemodialysis, rheumatoid arthritis, diabetes, and *S. aureus* nasal colonization are all associated with an increased risk of invasive infection.[33]

Coagulase-negative Staphylococcus species. A huge number of microorganisms of this group are ubiquitous members of the human microbiome found on the skin. *Staphylococcus epidermidis* is the most frequently identified member of this group. This species causes PJI primarily through its ability to adhere to prosthetic materials and produce

biofilm, although other more typical virulence factors have been identified more recently.[34,35] Other species that have been reported to cause PJI include *Staphylococcus simulans*, *Staphylococcus caprae*, and *Staphylococcus lugdunensis*. With the exception of *S. lugdunensis*, oxacillin resistance is found in the majority of PJI-associated *coagulase-negative staphylococci*.[36] *Coagulase-negative Staphylococcus species* can cause PJI at any time after an arthroplasty has been placed and are the second most common cause of early-onset PJI.

Streptococcus species. *Streptococcus* is a diverse genus that has a prominent role in human disease but only causes 10% of joint arthroplasty infections. A number of beta-hemolytic *Streptococcus* species cause PJI, including the Lancefield groups. *Streptococcus bovis* biotype I may cause PJI and is also associated with underlying colorectal neoplasia.[37] *Viridans* group *streptococci* are uncommon causes of PJI,[13] even after invasive procedures, such as upper endoscopy.[38] *Streptococcus pneumoniae* is also a rare cause of PJI.[39]

Enterococcus species. While rare causes of PJI overall, *enterococci* are found in up to 12 to 15% of patients with early-onset PJI, often as part of polymicrobial infections.[40,41] The source of the infecting organism was not described but was presumably hematogenous seeding from the gastrointestinal or urinary tract.

Aerobic Gram-negative bacilli. Much like *enterococci*, *aerobic Gram-negative bacilli* are more common in early-onset PJI, where they are found in up to 45% of infections in some studies.[40,41] They also play a prominent role in polymicrobial infections and may be a cause of hematogenous infection, which tends to be monomicrobial. In most studies, the most commonly isolated aerobic Gram-negative bacillus is *Escherichia coli*,[42,43] although it was *Pseudomonas aeruginosa* in one large study.[44] Due to the virulence of many *aerobic Gram-negative bacilli*, an acute presentation is commonly observed. Patients with PJI caused by aerobic Gram-negative bacilli tend to be older than those with PJI caused by Gram-positive bacteria.[44] Additionally, one small study reported that *aerobic Gram-negative bacilli* were more likely to occur in a hip rather than a knee

prosthesis.[42] This is possibly due to the proximity of the hip to the gastrointestinal tract.

P. acnes is a relatively low-virulence, anaerobic, *Grampositive bacillus* normally found on the human skin and sebaceous glands. This microorganism is typically inoculated at the time of surgery. This is a challenging organism in clinical practice, given that it may be more difficult to isolate and may have fewer associated clinical manifestations of infection than other bacteria. For example, many patients with *P. acnes* PJI have normal preoperative erythrocyte sedimentation rate (ESR) and C-reactive protein (CRP) values, even when rigorous nonmicrobiological findings suggestive of infection are present.[45] Additionally, acute inflammation is not uniformly present.[46]

2.2.2 Biofilm Role

A biofilm is any group of microorganisms in which cells stick to each other on a surface (Figure 3). These adherent cells are frequently embedded within a self-produced matrix of extracellular polymeric substance (EPS). They may be monomicrobial or polymicrobial, but even monomicrobial biofilms, especially those that are long-standing, may consist of subpopulations of the same organism with different phenotypic and/or genotypic characteristics. Some organism types grow together better than others in biofilms, which may impact the species found in polymicrobial biofilms.

The biofilm growth state is not static but rather consists of "stages," including attachment of microbial cells to a surface, initial growth on the surface, maturation of the biofilm, and, ultimately, detachment. Mature biofilms have a multicellular nonhomogeneous structure in which their component microbial cells may communicate with one another (e.g., through quorum sensing), and different subpopulations may have different functions, together supporting the whole biofilm and rendering biofilms somewhat analogous to a multicellular organism. While the biofilm phenotype evolved long before the advent of medical devices and in response to a need to grow on surfaces other than medical devices, the

ability to form biofilms equips certain bacteria and fungi with the capacity to cause medical device-associated infections, including PJI. Biofilm formation also explains why some normal flora organisms traditionally considered "harmless" become pathogens when they grow in the presence of foreign bodies.

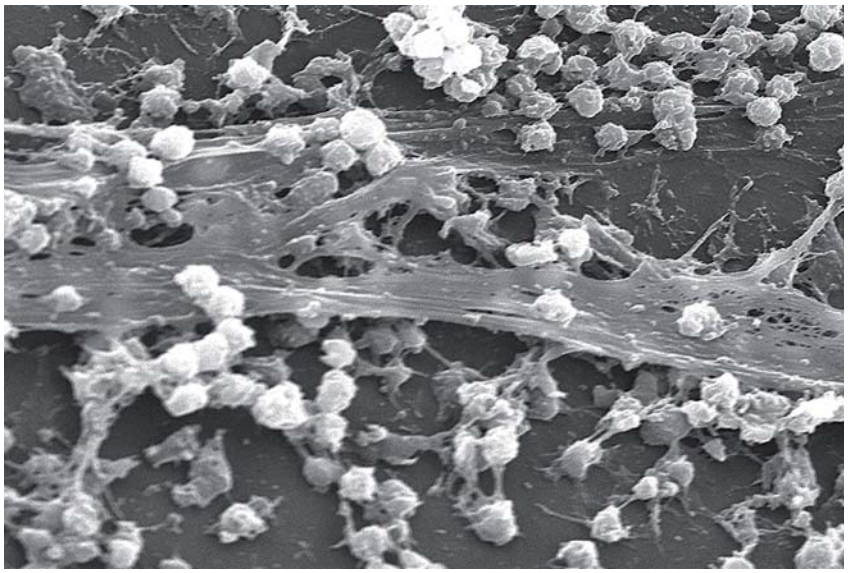

Figure 3. Staphylococcus aureus biofilm on a indwelling catheter. From reference[47].

In the biofilm state, bacteria are protected from antimicrobials and the host immune system,[47] making treatment of infection difficult without a biofilm-directed treatment strategy, which today mandates surgical intervention. In many cases, this may include prosthesis removal, to achieve a cure. The reduced antimicrobial susceptibility of bacteria in biofilms is related to their low growth rate, the presence of resistant bacterial subpopulations (so-called "persisters"), and a microenvironment within the biofilm that impairs antimicrobial activity.[48,49] Select antimicrobial agents such as rifampin may have activity against certain types of biofilms (e.g., staphylococcal biofilms). Moreover, bacteria in biofilms may impact on microbial culturing, producing false negatives, due to their low growth rate.[45,48]

Beyond the implications of biofilm formation for PJI pathogenesis and treatment, biofilm formation impacts the diagnosis of PJI. In particular and

especially in delayed- and late-onset PJIs, the implicated organisms are concentrated on the surface of the prosthesis and thereby limits the sensitivity of periprosthetic tissue and fluid cultures. One strategy to overcome this limitation is to sample the prosthesis surface itself, for example, by using device vortexing-sonication.

2.3 Diagnosis

For many years, research on PJI has been limited by a lack of standardized diagnostic criteria. This limitation must be considered when interpreting the PJI literature. Over the last several years, several groups that include the Infectious Diseases Society of America (IDSA) and the Musculoskeletal Infection Society (MSIS), have published proposed or accepted definitions for the diagnosis of PJI.[28,50] Additionally, the European Bone and Joint Infection Society (EBJIS), the American MSIS, and a number of other organizations from around the world recently held an international consensus meeting in an attempt to refine the definition of PJI.[51] The MSIS PJI definition is similar to the Duke criteria for endocarditis, with major or definitive criteria for PJI diagnosis as well as minor or supportive criteria.[28] Definitive evidence of PJI is a sinus tract in communication with the prosthesis or an identical pathogen found in two separate periprosthetic tissue or fluid samples.

Nevertheless, as already mentioned above, PJI diagnosis remains a complex procedure based upon a combination of clinical findings, laboratory results from peripheral blood and synovial fluid, microbiological data, histological evaluation of periprosthetic tissue, intraoperative inspection, and, in some cases, radiographic results. It is important to emphasize that there is currently no diagnostic method or test that is accurate enough for PJI.

Three important questions must be answered for the correct diagnosis and treatment of PJI:

1. Is the joint infected?
2. What is the causative microorganism?

3. What is the antimicrobial susceptibility of the causative microorganism?

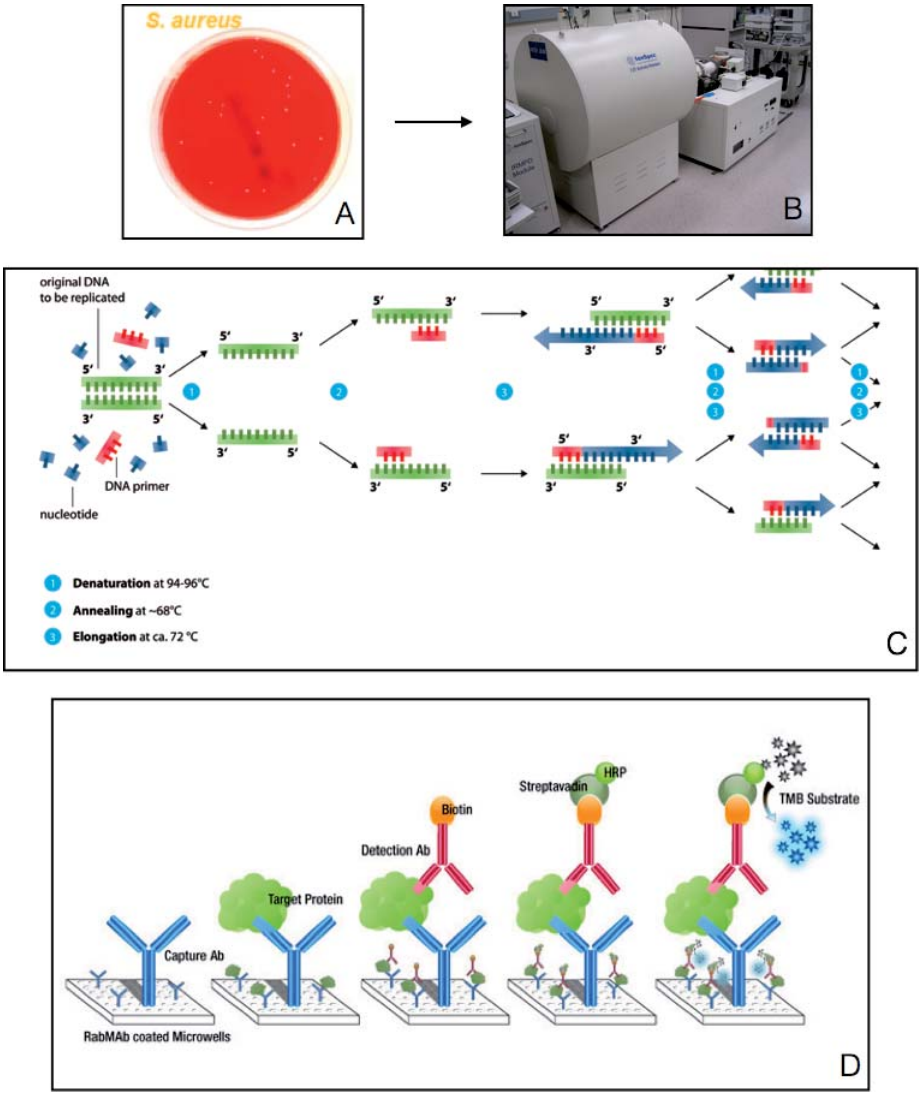

Figure 4. Some examples for the actual detection of microorganisms in clinical diagnosis: (A) Cell culture, (B) Mass spectrometry of isolated pure colonies (C) polymerase chain reaction, and (D) enzyme-linked immune sorbent assay.

Peripheral blood tests that rely upon assessing the host response to the infecting pathogen, *erythrocyte sedimentation* and *C-reactive protein* which are the most frequently used inflammatory markers and computed tomography and magnetic resonance which allows high spatial resolution

are only useful to answer the question *1*. Besides, these tests are limited by a low sensitivity or specificity.[14,52] On the other hand, the most frequently used procedures to identify what the causative microorganism of PJI in a patient is (*question 2*) include: Synovial fluid culture, preoperative periprosthetic tissue biopsy, intraoperative periprosthetic tissue culture and sonication of removed prosthetic components, among others. All of these procedures pass through conventional microbial typing methods that suffer from inherent time-consuming complexities. Among these methods, the most usual in many labs is still the culture of the microorganism in different media to isolate the species and identify its nature (Figure 4A). Sequential cultures can be avoided by implementing mass spectrometry (MS) techniques for the identification of isolated pure colonies (Figure 4D). These methods, including the identification by MS requires time for the agent to grow (4-14 days or more).[15] On the other hand, immunological tests to identify microorganism are also popular. Immunological techniques such as enzyme-linked immune sorbent assay (ELISA, Figure 4C), fluorescence immune assay (FIA) or radioimmunoassay (RIA) offer faster results but cannot be considered multiplex and require a considerable amount of sample. Alternatively, some labs are introducing the polymerase chain reaction (PCR) to identify microorganism through the profiling of their genetic code (Figure 4B). This technique is quantitative and semimultiplex. No matter, it is laborious, slow (1-5 h) and expensive (50-250 € per assay). Overall, it can be concluded that the current methods for detection of microorganism are flawed of problems related to sensitivity, speed, price and technological restrictions. In this scenario, Surface enhanced Raman Scattering (SERS)[53] offers an exceptional opportunity for the development of new sensing devices amenable to implementation quantitative multiplex analysis in real time.

2.4 Treatment

PJI treatment is a complex procedure that requires surgical intervention and medical therapy in the majority of cases. While surgical manegement occur in the hospital, most of the antimicrobial treatment is given following

hospital discharge. Accordingly, the best outcomes can be expected when a collaborative relantionship exists between orthopedic surgeons and infectious disease doctors.

The goal of PJI treatment is to eradicate the infection providing pain relief and restoring the function of the infected joint. Unfortunately, this goal cannot be achieved for every patient. Various therapies have been used to treat PJI. That includes surgical removal of all infected tissue and the implant, a combination of débridement with implant retention and a long-term antimicrobial therapy that is active against biofilm microorganisms. Long-term therapy with suppressive antimicrobial agents is practically the only way for patients in whom surgery is contraindicated.[54]

There is some variability in the antimicrobial treatment. For most patients, antimicrobials are held prior to surgery if the microbiology result is undetermined. Broad-spectrum therapy is typically indicated in the immediate postoperative period if the causative microorganism(s) and antimicrobial susceptibility test results are not known. Therefore, the identification of the infectious agent and the determination of its antimicrobial susceptibility are crucial to tailor an antimicrobial therapy. Most clinicians use intravenous antibiotics for the first 2 to 6 weeks followed by a regimen of debridement, antibiotics, irrigation, and retention of the prosthesis (DAIR).[55–57] This procedure should be performed by using open arthrotomy. A surgical incision is opened followed by irrigation and debridement of any necrotic or infected soft tissue, removal of any hematoma and evacuation of any purulence surrounding the prosthesis. Besides, many clinicians use oral antibiotic suppressive therapy for some period of time following the initial treatment course, given the difficulty in eradicating surface-adhering, slow-growing, and biofilm-producing microorganisms.[47,58–60] As an example, Rifampin is an antimicrobial agent that has bactericidal activity against sthaphylococci that grow in biofilms.[61] Rifampin should never be administered alone, since staphylococci rapidly develop antimicrobial resistance.[62] Quinolones are excellent combination agents because their bioavailability, antimicrobial activity, and tolerability. Unfortunately, High-quality data to support one particular antimicrobial

strategy over another do not exist but may depend upon the virulence of the infecting pathogen, the antimicrobial therapy provided in the initial postoperative period, the antimicrobial susceptibility profile and availabity of oral therapy, and the consequences if treatment failure occurs.

On the other hand, a drastic surgical therapy should be performed in the worst cases. This may include removal of all foreign material and reimplantation of a new prosthesis, permanent removal of the prosthesis and debridement without reimplantation or amputation.

2.5 Raman Scattering

Raman scattering (RS) is the inelastic part of the light scattered by a molecule when illuminated. This process is known as the Raman effect, and was theoretically postulated in 1923 by A. Smekal *et al.*[63] and experimentally demonstrated in 1928 by C.V. Raman.[64] The interaction of light with matter can be of different types, but we shall mainly focus on absorption or scattering phenomena to explain the basis of the Raman effect. Absorption occurs when the energy of the incident photon corresponds to the energy gap between the ground state of an atom or a molecule and an excited state. The photon may be absorbed and the molecule will be promoted to an excited state of higher energy. Scattering may occur in the case when the energy of the incident photon does not correspond to a specific energy level of an excited state of an atom or a molecule upon illumination.

The predominant part of the photons are elastically scattered in a process called Rayleigh scattering. Rayleigh scattering takes place when the electron cloud relaxes without any nuclear movement. This is essentially an elastic process and there is no appreciable change in the energy of the photon. On the other hand, a very small fraction of the scattered light, one in a 10^6-10^8 photons, undergoes inelastic scattering in the process known as Raman scattering. This process results in a scattered photon with different frequency to that of incident photon. This phenomenon occurs when the light and the electrons interact and result in a movement of the nuclei. As the nuclei are much heavier than the

electrons, there is an appreciable change in the energy of the molecule to either lower or higher energy depending on whether the process starts with a molecule in the ground state (Stokes scattering) or from a molecule in a vibrationally excited state (anti-Stokes scattering). Figure 5 shows a simple diagram illustrating Rayleigh and Raman scattering.

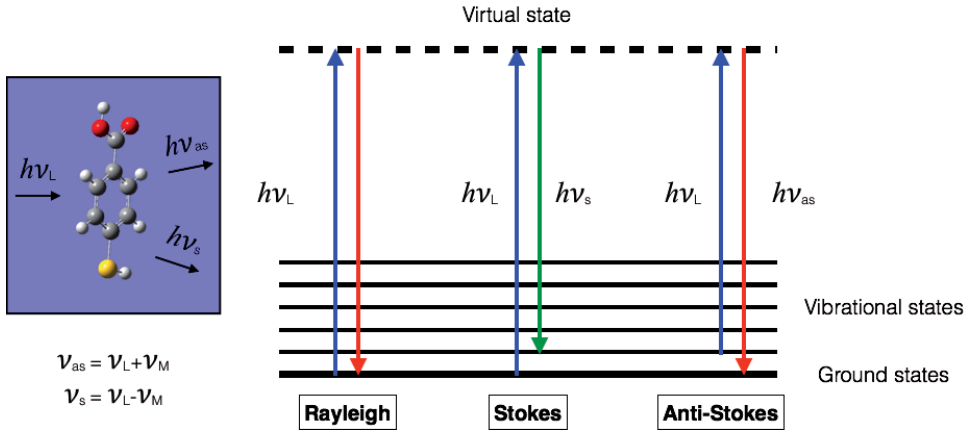

Figure 5. Diagram of the Rayleigh and Raman scattering processes.

Light shifted lower than the excitation energy (Stokes scattering) has an energy of $h\nu_s = h\nu_L - h\nu_m$; and light shifted higher (anti Stokes scattering) has an energy of $h\nu_{as} = h\nu_L + h\nu_m$; where $h\nu_m$ is the molecule's vibrational energy. The wavenumber shown in a Raman spectrum represents the frequency shift between excitation photon and scattered photon. Therefore, the position of a Raman band will not change if a different excitation wavelength is applied.

Experimentally, the spontaneous inelastic Raman scattering, the total Stokes scattered light, is averaged over all the random molecular orientations, where $I_{RS}(\nu_s)$ (photons s^{-1}), is proportional to the incoming flux of photons, $I_0(\nu_L)$ (photons s^{-1} cm^{-2}): $I_{RS}=\sigma_{RS} \cdot I_0$. The proportionality constant, the Raman cross-section (σ_{RS}), has the dimensions of area and is a function of the energy of the excitation light. The Raman cross-section is proportional to the square of the polarizability derivative for the $m \rightarrow n$ vibrational transition and the fourth power of the scattering frequency. The efficiencies of the absorption and scattering processes are determined by the function "cross-section", which is the meeting point of experiments with

theory. The cross-section is different for each atom or molecule and for each analytical technique.

2.5.1 Raman scattering cross-section

To better understand Raman scattering, it is interesting to discuss the Raman scattering cross-section more in-depth. The first step is to quantify how many incident photons are scattered through Raman or Rayleigh processes. By definition, for a given linear optical process suffered by a molecule, the *cross-section*, σ (m^2), is the quantifiable variable that relates the signal produced by this process to the incident power density at the molecule position as:

$$P = \sigma \cdot S_0$$

Equation 1

where P is the intensity or power of the signal produced by the optical process (proportional to the number of photons per unit time involved in the process) and S_0 ($W \cdot m^{-2}$) corresponds to the incident power density.

Because scattering is not a linear optical process, the Equation 1 does not fully describe the scattering process. For that reason, it is interesting to know how many photons are scattered in a specific direction; this variable is called the *radiation profile* and relates to the scattering efficiency. The *radiation profile* can be characterized by the angular dependence of the scattered power. In 3D processes, the single variable $\Omega = (\theta, \phi)$ specifies a direction. If we apply this definition to a Raman scattering process, this double angular dependence of the scattered power can then be formally defined as $dP_{Sca}/d\Omega$ ($W \cdot sr^{-1}$), which is a function of Ω, and is called the *differential scattered power*. By analogy with the previous definition, it is possible to define a *differential scattering cross-section*, $d\sigma_{Sca}/d\Omega$ ($m^{2} \cdot sr^{-1}$), also a function of Ω along the following expression:

$$\frac{dP_{Sca}}{d\Omega}(\Omega) = \frac{d\sigma_{Sca}}{d\Omega}(\Omega) \cdot S_0$$

Equation 2

The function $\frac{d\sigma_{Sca}}{d\Omega}$ characterizes the *radiation profile* of the scattering process. Since the total scattered power should be the sum of the scattered power in all directions, we have a relationship between the *scattering cross-section* and the *differential scattering cross-section* in the form of:

$$\sigma_{Sca} = \int \frac{d\sigma_{Sca}}{d\Omega}(\Omega) \cdot d\Omega$$

Equation 3

In the particular case of the Raman scattering process, several additional considerations to make the above general scattering cross-section expressions more precise are needed.[65] Taking into account that the scattered radiation is detected in a particular direction, usually 90° or back-scattering, and in order to summarize the tedious theoretical treatment, we only present here the final mathematical expression that defines the *absolute differential Raman cross-section* (implicitly for a Stokes process*)* $\frac{d\sigma_{RS}}{d\Omega}$ ($m^2 \cdot sr^{-1}$):

$$\langle I_{RS} \rangle = \frac{d\sigma_{RS}}{d\Omega} S_0 \cdot \delta\Omega$$

Equation 4

where $\delta\Omega$ (sr) is the small solid angle for light collection, which in turn is related to the numerical aperture of the collecting optics. The Raman scattered intensity $\langle I_{RS} \rangle$ (W) is the signal obtained for a given vibrational mode of a single molecule, averaged over all orientations of the molecule in space.

According to Equation 4, the *absolute differential Raman cross-section* depends on the vibrational mode for a given molecule, the excitation wavelength and the medium in which the molecule is dissolved.

2.5.2 Resonance Raman scattering

Resonance Raman scattering (RRS) is a phenomenon that takes place when the energy of the incident light is close to the frequency of a molecular electronic transition. In this case, the energy of the virtual state is

resonant (same energy) with one of the electronic levels in the molecule, resulting in an enhancement of the scattering efficiency of the molecule. This effect is observed in molecules that absorb in the vicinity of the incident laser wavelength. Many common probes in SERS (such as dye molecules) are used precisely because they have such electronic resonance contribution in the visible (chromophore) and, accordingly, have large Raman cross-sections.

2.6 Surface-enhanced Raman scattering (SERS)

The application of nanostructured materials toward the development of novel detection techniques with improved sensitivity or simplified and faster applicability has rapidly become an appealing alternative to other technologies. Among them, SERS is a powerful analytical technique which has already proven to be particularly effective in many fields of science (i.e., environmental detection and monitoring applications).[21,22,53,66–71] Essentially, SERS can be described as Raman scattering amplified by the presence of a plasmonic structure in the close vicinity of the target analyte. The central topic of plasmonics, and hybrid term of plasma oscillations (plasmons) and electronics, involves the optical properties of metal nanostructures. As Raman scattering, SERS provides a complex spectral pattern that contains all the compositional and structural characteristics of the molecule under study.[72] Moreover, SERS is also characterized by an extreme experimental flexibility since Raman measurements can be carried out over a wide spectral range, are insensitive to air and water and require no sample preparation.

Therefore, not only the interaction between light and molecules/matter need to be considered for understanding SERS, the interaction between light and metal nanostructures also has and important role.[20,73] SERS produces a remarkable amplification of the Raman signal by several orders of magnitude with enhancement factors $>10^6$ and it is due to two mechanisms (Figure 6). An effect known as *electromagnetic enhancement* (see section 2.6.2) increases the Raman signal by the magnification of both incident and Raman scattered fields. On the other hand, the electronic

interaction between the molecule and the metal can modify the scattering process itself and produce an effectively larger cross-section than would occur by light scattering from the molecule alone, an effect known as *chemical enhancement* (see section 2.6.3).

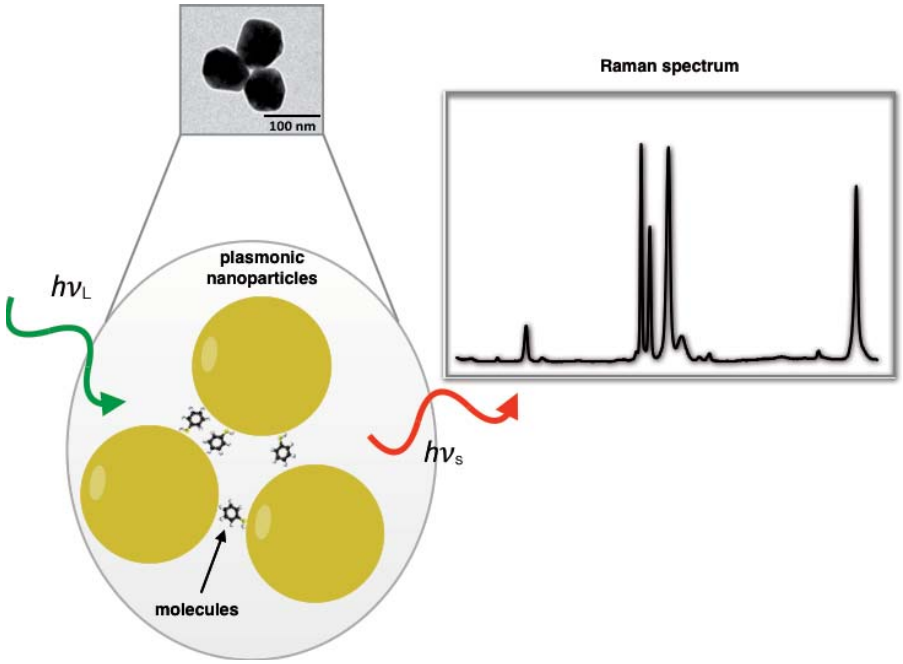

Figure 6. (A) Molecules are adsorbed onto the surface of metallic nanostructures (yellow spheres). The SERS spectrum reveals molecular-vibration energies based on the frequency shift between the incident (green line) and the scattered light (red line).

To summarize, SERS is a molecular spectroscopic technique that is based on the plasmon-assisted scattering of molecules on or near metal nanostructures. Molecules are therefore an intrinsic and integral component of SERS and it is this wealth of chemical/molecular, and to certain extent also structural information, which makes SERS such a powerful technique. In other words, there is no SERS without molecules, but there is also no SERS without plasmonic nanostructures.

2.6.1 Plasmonic nanostructures

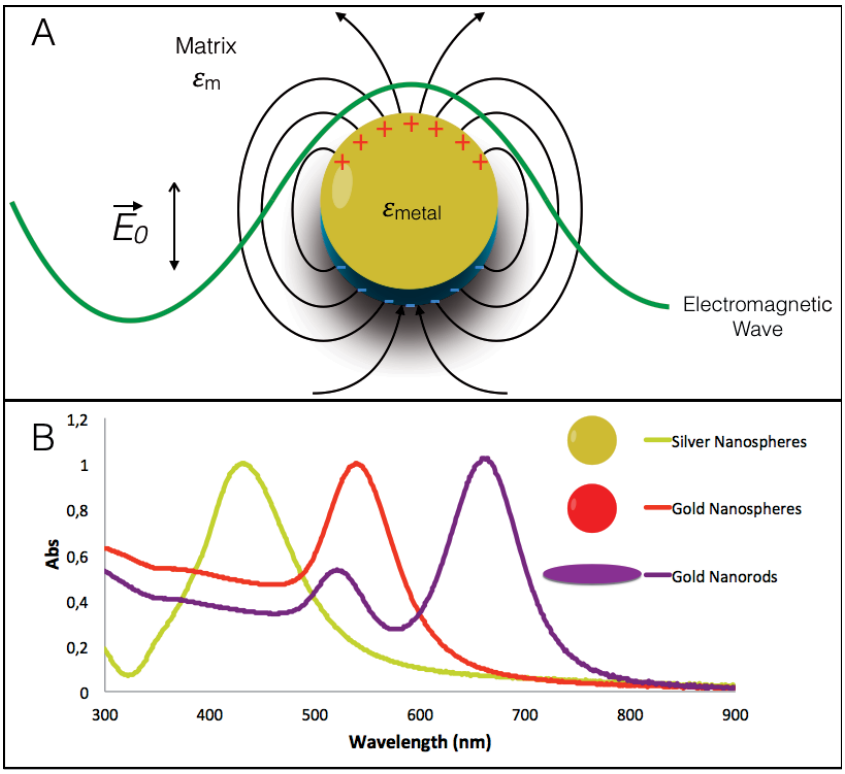

Figure 7. (A) Representative scheme depicting the induction of a localized surface plasmon resonance in a noble metal sphere nanoparticle upon excitation with an electromagnetic radiation. An electric dipole is created in the small spherical particle, whereas the oscillation of the electron cloud can occur along any of the two symmetry axes. The resonance frequency (ω_{max}) of the plasma oscillations in the metal nanostructure depends on the dielectric functions of the metal $\varepsilon_{metal}(\nu)$ and the surrounding medium $\varepsilon_m(\nu)$ (B) Experimental LSPR bands in the UV-Vis-NIR of (yellow line) silver nanospheres, (red line) gold nanospheres, and (violet line) gold nanorods.

For practical quantitative analytical applications, SERS, as a tool, must fulfill the typical requirements of an analytical technique: reproducibility of the results, linearity of the response, standardization and molecular selectivity. Unfortunately, these requirements are not easily met in the case of SERS experiments. Chemical and electronic effects have to be carefully controlled in order to bring SERS as close as possible to the basic analytical requirements. Nevertheless, during the last 15 years, the preparation of

SERS substrates has become more controllable, benefiting from the development of nanoscience and nanotechnology. In such a case, noble metal nanoparticles in suspension, predominantly made of Ag or Au due to their strong SERS activity and reasonable chemical stability, represent one of the simplest and easiest route to SERS for their versatility and easy synthesis with a high degree of control over the composition, shape and size.

The most important property of these nanostructures is the so-called *localized surface plasmon resonance* (LSPR) which is generated by the collective oscillation of the conduction band electrons upon excitation with the appropriate electromagnetic field (i.e., laser).[74,75] As a consequence of this excitation a high electromagnetic field is created at the surface of the nanoparticle which can be applied for the enhancement of spontaneous Raman scattering of the molecular species placed in close vicinity to this surfaces. More specifically, when a small spherical metal nanoparticle is irradiated by light, the oscillating electric field originates a coherent motion of the conduction electrons (Figure 7). When the electron plasma is displaced relative to the position of the ionic background (*e.g.* Au^{n+}), a restoring force arises from Coulomb attraction between electrons and the positively induced charge, resulting in oscillations of the electron cloud relative to the position framework. Providing that the metallic sphere is smaller than the wavelength of the incident radiation, the collective oscillation of the electrons is dipolar in nature. Thus, the resonance condition for the coherent electronic motion with the electric field is unique, which is observed experimentally as a single plasmon band in visible spectroscopy (Figure 7B). While for most metals these resonances take place in the UV, for metals like gold, silver, copper and others, the LSPRs are located in the visible region of the electromagnetic spectrum and they are therefore suitable for the visible and NIR excitation lines commonly used in Raman scattering. Moreover, the surface plasmon absorption of nanoparticles can be shifted depending on the size, shape, composition and nature of the surrounding medium.[76,77]

On the other hand, non-spherical noble metal nanostructures generally exhibit more than one plasmonic resonance, which are the result from electron dipolar oscillations in different directions. As an example, in the case of gold nanorods two different surface plasmon resonances can be produced, which are called transversal and longitudinal modes, and correspond to the electronic oscillations perpendicular and parallel to the long axis (Figure 7B).

2.6.1.1 The Mie-Drude Theory for spheres

To interpret the experimental observations and relate the optical properties to the particle structure, it is important to predict the plasmon resonance frequencies theoretically. In 1908, Mie[78] was the first who explained the red color of gold nanoparticle solutions. The combination of Mie's theory with the Drude model made it possible to solve Maxwell's equations for an electromagnetic light wave interacting with a small metal sphere surrounded by a dielectric medium. This theory is only valid for spherical particles, but there are modifications like the Gans–Mie[79] theory, which allows for the calculation of the optical properties of ellipsoidal particles.

The origins and behavior of the optical effects displayed by nanosized metal particles in diluted solutions can be explained by combining the classical Drude model to describe the dielectric properties of metals with the Mie theory for light absorption and scattering by spheres. The mechanism for the absorption of light by small metal particles is based on the assumption that the plasma oscillation of the collective conduction electrons of the particles is caused by the restoring force resulting from the induced charge separation on the surface of the particle during the interaction between the electromagnetic field and the particle. Such absorption of light in the UV-VIS region by metal particles is sensitive to the particle size,[74,80,81] shape,[82–86] dispersion medium,[74,87,88] particle material,[84] encapsulating layers,[89] electron density at the particles surface,[89–91] and temperature.[86]

The optical properties of small spherical colloids can be properly calculated by Mie theory.[78] For instance, a dispersion with well separated particles and homogeneous dielectric properties will be considered to be described by this theory. The absorbance, *A*, of light occurs as the irradiance of a beam of light is exponentially attenuated from I_0 to I_t in traversing a distance l through a dilute solution containing *N* particles per unit volume, expressed by:

$$A = -log_{10}\left(\frac{I_t}{I_0}\right) = \frac{NC_{ext}l}{2.303}$$

Equation 5

where C_{ext} is the extinction cross section of a single particle, which results from both the scattering and absorption of light by the particle. Although both processes occur simultaneously, there are instances where one or the other dominates. For particles which are very small compared with the wavelength of light, only absorption is significant. For the purpose of this work we only consider particles in the nanosize regime, in which scattering is negligible. By using the complex expression for the dielectric constant (Equation 6), Mie[78] calculated the extinction cross section, C_{ext}, of a solution of diluted small spherical metal particles embedded in an isotropic, non-absorbing medium of dielectric constant $\varepsilon_m = {n_m}^2$ to be:

$$\varepsilon(\lambda) = \varepsilon'(\lambda) + i\varepsilon''(\lambda)$$

Equation 6

$$C_{ext} = \frac{2\pi}{m^2}\sum_{n=1}^{\infty}(2n+1)Re(a_n + b_n)$$

Equation 7

where $m = 2p/l$ is the wavenumber, and a_n and b_n are the scattering coefficients which are functions of the particle radius *R* and the incident wavelength l in terms of Ricatti-Bessel functions. Based on the dipole approximation, for spherical particles very small compared with the wavelength of light ($2pR/l << 1$) whereby scattering is insignificant, only the first, electric dipole term in Equation 7 is important, and C_{ext} is reduced to

$$C_{ext} = \frac{24\pi^2 R^3 {\varepsilon_m}^{3/2}}{\lambda} \frac{\varepsilon''}{(\varepsilon' + 2\varepsilon_m)^2 + \varepsilon''^2}$$

Equation 8

where ε' and ε'' are the real and imaginary parts of the complex dielectric function of the metal particle. Other assumptions made, for Equation 7 to be valid, are that the particles be monodisperse and isolated. That is, the separation between the particles must be larger than ca. 10 particle diameters; thus in the case of 10 nm particles, this corresponds to a maximum concentration of ~ 10^{15} particles/dm^3. Equation 8 determines the shape of the absorption band of the particles, with the width and height of the resonance. Given that it is small or does not change greatly within the vicinity of the absorption band, the position of the maximum absorption occurs when

$$\varepsilon = -2\varepsilon_m$$

Equation 9

From Equation 8, two limiting cases can occur, where C_{ext} is zero. In the first case, the complex part for the dielectric constant is zero ($\varepsilon'' = 0$), and then the material is not absorbing radiation. In the second case, $\varepsilon'' = \infty$, and the material reflects all incoming radiation at this wavelength. As can be also seen from Equation 8, the extinction coefficient does not depend on particle dimensions, but size dependence is observed experimentally.[81,92–94] This is because electron density becomes very small. Obviously, the assumption of bulk-like electronic bands and bulk electronic and optical properties associated with the electronic structure of the nanoparticles is rather questionable. In particular, the use of the bulk dielectric constant which enters the Mie equation as the only material-related physical quantity is not justified any longer.[81] However, as Mie theory has been very successful in describing the optical absorption spectra of metal nanoparticles,[74] the theory was modified to account for the size effects in combination with the Drude model. The first correction is to assume that the dielectric constant of the material is size dependent below an average particle diameter of about 20 nm.[81] Due to that, the smaller the

particles, the faster the electrons reach the surface of the particles. The electrons can then be scattered at the surface and lose coherence more quickly than in a larger nanoparticle. Therefore, the plasmon bandwidth increases with a decreasing nanoparticle radius. This effect is included in the calculation by applying the Drude model, taking into account the reduction of the effective electron mean free path and enhanced electron-surface scattering.[95,96] Then, the real and imaginary dielectric components in $\varepsilon = \varepsilon' + i\varepsilon''$ are functions of frequency. According to the Drude model26 the real and imaginary parts of the complex dielectric function, *e*, may be related to the light angular frequency $\omega = 2\pi\nu$ as

$$\varepsilon' = \varepsilon^{\infty} - \frac{{\omega_p}^2}{\omega^2 + {\omega_d}^2}$$

Equation 10

and

$$\varepsilon' = \frac{{\omega_p}^2 \omega_d}{\omega(\omega^2 + {\omega_d}^2)}$$

Equation 11

where ε^{∞} is the high frequency dielectric constant, ω_p is the plasma frequency given by

$${\omega_p}^2 = \frac{Ne^2}{m\varepsilon_0}$$

Equation 12

in terms of the electron concentration *N*, electron charge *e*, electron mass *m* and permittivity of vacuum ε_0. is ω_d the scattering frequency, which for the bulk metal is given by

$$\omega_d = \frac{\nu_F}{R_{bulk}}$$

Equation 13

where ν_F is the velocity of conduction electrons at the Fermi level, and R_{bulk} is the mean free path of conduction electrons in the bulk metal. The

scattering of free electrons is directly related to the metal conductivity (σ) in the Drude formalism by

$$\sigma = \frac{Ne^2 R_{bulk}}{m v_F} = \frac{Ne^2}{m\omega_d}$$

Equation 14

For particles within the 3-20 nm diameter size range there is not a strong dependence of the absorption spectra on the particle size. This is because the quadrupole and higherorder terms in the Mie summation become significant only when particles are larger than 20 nm. However, the spectra of some metal colloids below this size range do show a size dependence due to the collision of conduction electrons with the particle surface becoming more appreciable as the particle radius, *R*, becomes smaller than the mean free path in the bulk metal, $1/R_{bulk}$. Consequently, the effective electron mean free path, R_{eff}, then becomes size dependent as

$$\frac{1}{R_{eff}} = \frac{1}{R} + \frac{1}{R_{bulk}}$$

Equation 15

which means,

$$\sigma(R) = \frac{Ne^2 R}{m v_F}$$

Equation 16

This was verified by Kreibig for gold and silver particles.[81] Kreibig demonstrated that decreasing *R* increases ω_d which consequently both broadens the surface plasmon band and decreases its intensity but causes only a very small shift in the peak position. This effect is most marked for metals with relatively long electron mean free paths such as the alkali metals, copper or silver yet is small for most other metals.

However, plasmon resonance depends explicitly on the particle size for larger nanoparticles (>20 nm in the case of gold) where the dipole approximation is no longer valid. Therefore, the plasmon band red shifts with increasing particle size. Using Equation 8, the optical properties of

spherical metal particles can be suitably calculated from either sets of the optical constants, the real and imaginary parts of the complex dielectric function, $\varepsilon = \varepsilon' + i\varepsilon''$, or the complex refractive index $N = n + ik$. Analogous to the complex dielectric function, the real part, n, of the refractive index determines the wavelength in the medium and the imaginary part k, the absorption coefficient. The complex index of refraction can also be related to the complex dielectric function as

$$\varepsilon = \varepsilon' + i\varepsilon'' = (n + ik)^2$$

Equation 17

$$\text{i.e} \quad \varepsilon^2 = n^2 - k^2 \quad \text{and } \varepsilon'' = 2nk$$

Equation 18

2.6.2 Electromagnetic enhancement in SERS

It is generally accepted that the main contribution to the increase of the Raman signal arises from the intense local electromagnetic fields generated by an efficient coupling between the localized surface plasmon resonance of a nanostructure and the incident radiation.[20] The more rigorous expressions for the electromagnetic enhancement factor were described by Kerker.[97] Due to the highly complicated mathematical treatment that is necessary to come across them, in this section an overview from a practical standpoint is provided by taking a simple spherical particle model of the SERS electromagnetic mechanism (EM).

The magnitude of the dipolar field (E_{sp}) radiated by the metallic nanosphere at a nearby molecule depends on the sphere's radius r, its distance d from the molecule, the dielectric constants of the metal $\varepsilon_{\text{metal}}$ and the surrounding medium ε_m, and the incident field strength E_0 (see Figure 8).

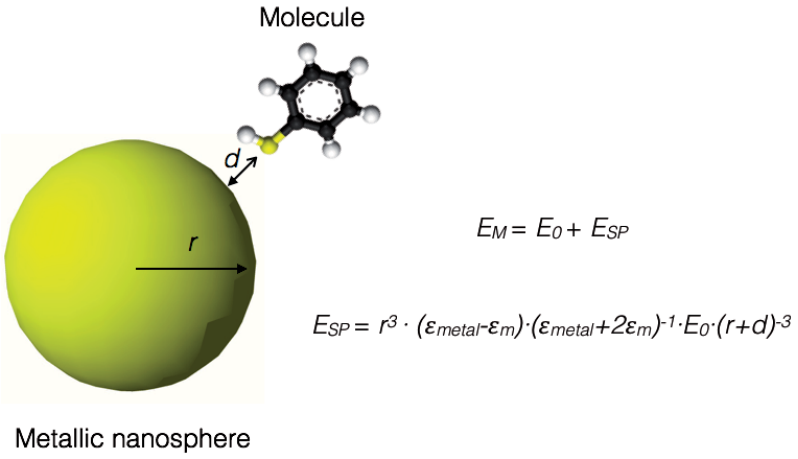

Figure 8. Diagram of electromagnetic mechanism for SERS enhancement.

Therefore, the molecule feels an enhanced local field (E_M) which includes both electric-field magnitudes: E_0 + E_{SP}. The light field enhancement A(ν) is determined by the ratio between the field at the position of the molecule and the incoming field.

$$A(\nu) = \frac{E_M(\nu)}{E_0\,(\nu)} \approx \frac{\varepsilon_{metal} - \varepsilon_m}{\varepsilon_{metal} + 2\varepsilon_m} \times \left(\frac{r}{r+d}\right)^3$$

Equation 19

Where A(ν) is particularly strong when the real part of $\varepsilon_{metal}(\nu)$ is equal to $2\varepsilon_m(\nu)$. Additionally, for a strong electromagnetic enhancement, the imaginary part of the dielectric constant needs to be small. These conditions describe the resonant excitation of surface plasmons for a metal sphere. Similarly, the scattered field will be enhanced if it is in resonance with the particle LSPR. Thus, considering the enhancing effects for the laser and the Stokes field, the electromagnetic SERS enhancement factor G^{SERS} (ν_s) can be expressed as:

$$G^{SERS}(\nu_s) = |A(\nu_l)|^2 |A(\nu_s)|^2 \approx \left|\frac{\varepsilon(\nu_L) - \varepsilon_0}{\varepsilon(\nu_L) + 2\varepsilon_0}\right|^2 \left|\frac{\varepsilon(\nu_s) - \varepsilon_0}{\varepsilon(\nu_s) + 2\varepsilon_0}\right|^2 \left(\frac{r}{r+d}\right)^{12}$$

Equation 20

This equation shows that the enhancement scales as the fourth power ($|E|^4$ enhancement) of the local field of the metallic nanostructure and that it is particularly strong when excitation and scattered field are in resonance with the surface plasmons.

The $|E|^4$ approximation model is commonly used to explore the EM enhancement and considers the Raman scattering in the vicinity of the above defined metallic surface. A more detailed explanation of this model can be given by separately taking into account the enhancement of both the incident and the emitted radiation. According to that, the SERS electromagnetic enhancement factor (*EF*) can be simply expressed as:

$$EF \approx M_{Loc}(\omega_L) M^d_{Rad}(\omega_R)$$

Equation 21

where $M_{Loc}(\omega_L)$ is the local field intensity enhancement factor and $M^d_{Rad}(\omega_R)$ corresponds to the directional radiation enhancement factor (related to a given position). M_{Loc} characterizes how much the field intensity is with respect to the intensity if there were no metal substrate present. It can be found by solving the electromagnetic problem under specific external excitation conditions with an incident field E_{Inc}, which yields the local field E_{Loc} everywhere.

Estimating M^d_{Rad} is a priori a more difficult task, but in order to avoid further complications, it is often assumed that $M^d_{Rad}(\omega) \approx M_{Loc}(\omega)$. That means that the SERS enhancement can then be expressed as:

$$SMEF(\omega_L, \omega_R) \approx M_{Loc}(\omega_L) M_{Loc}(\omega_R) \approx \frac{|E_{Loc}(\omega_L)|^2}{|E_{Inc}|^2} \frac{|E_{Loc}(\omega_R)|^2}{|E_{Inc}|^2}$$

Equation 22

This expression has been widely used in the literature, and provides a fairly simple way of estimating the electromagnetic enhancement factor from a calculation of the local field at the excitation and Raman frequencies.

Moreover, in many cases, the Raman shift is also small and one can make the additional approximation that $\omega_R \approx \omega_L$.[98] This leads to the even

more famous expression of the SERS enhancement for zero-Stokes shift in the $|E|^4$ approximation as:

$$EF(\omega_L) \approx \frac{|E_{Loc}(\omega_L)|^4}{|E_{Inc}|^4}$$

Equation 23

In many instances, this approximation is sufficient to obtain the right order of magnitude of the EF. However, it is important to keep in mind that this approach only approximates the *radiation enhancement* and does not account for polarization effects or surface selection rules in SERS.[73,98]

The central message here is that very high local electrical fields are responsible for the significantly increased signal strength observed in SERS relative to normal Raman scattering. Maximum electromagnetic enhancement values for spherical silver and gold particles are around 10^6–10^8.[99,100] However, the theory predicts much higher enhancement of the electromagnetic fields for tips and high curvature regions. As an example, it has been demonstrated that the SERS electromagnetic enhancement factor can be increased to values near 10^{11} at the tips of star-shaped colloids.[101] Likewise, the interaction between particles situated at short distances (d→0) provides an additional enhancement of the field, generating the so-called 'hot-spots', a term that will be further explained in section 2.6.4. Accordingly, electromagnetic enhancement factors higher than 10^{11} have been estimated at the middle of the gap between two silver or gold spherical particles separated by 1 nm.[101]

2.6.3 Chemical enhancement (CE) in SERS

The EM mechanism describes the enhanced local electromagnetic fields due to resonant excitation of plasma oscillations in the metallic nanostructure. This purely physical effect is by far the most dominant contribution. Nevertheless, early observations revealed a dependence of the scattering signal on the electrode potential.[102] It suggests an electronic coupling between the molecule and the metal. In addition, the presence of metal in the system may alter the polarizability of adsorbed molecules and

increase the Raman-scattering efficiency. Moreover, if SERS was only an electromagnetic effect, an intense SERS signal should exist for every molecule in the vicinity of a plasmonic nanostructure. The higher EF predicted for the EM effect (10^{12}) presents a difference of two orders of magnitude with respect to the higher EF observed experimentally for non-resonant SERS (10^{14}).[103]

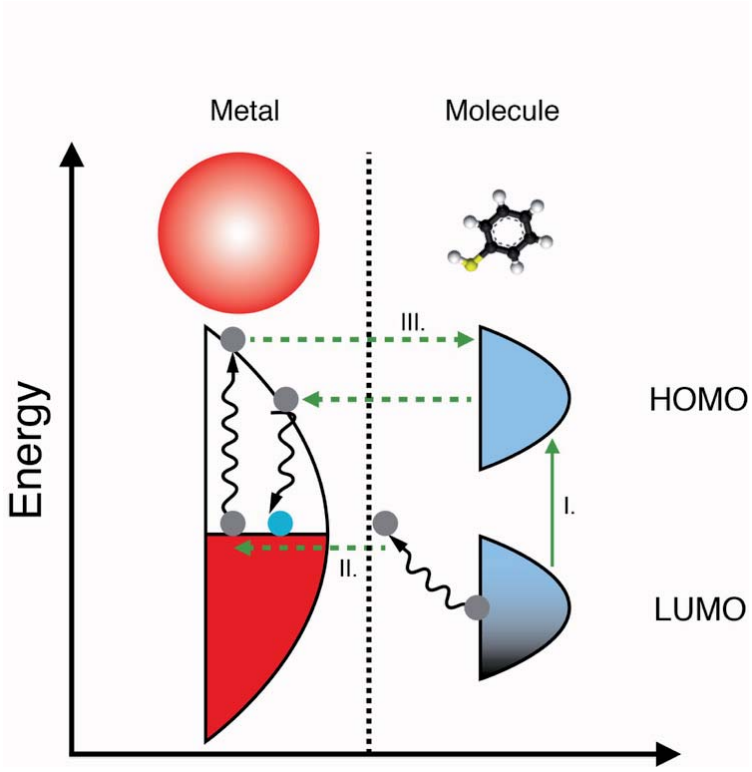

Figure 9. Energy level diagram for a "molecule-metal system" showing a possible transfer charge process involving molecular states (I) and molecular and metallic states (II, III).

Different mechanisms have been discussed as the origin of the "chemical" SERS effect (sometimes is also called *first-layer effect*). However, the important concept is that it will only contribute to the enhancement if there is contact between the molecule and the nanostructure.[104] The electronic coupling between molecule and metal and the formation of a surface complex leads to a *charge transfer* (CT) from the metal to the molecule or vice cersa and within the adsorbed molecule itself resulting in an increased Raman signal. The energies of the highest occupied

molecular orbital (HOMO) and the lowest unoccupied molecular orbital (LUMO) are approcimately symmetric relative to the Fermi level of the metal, together with the possible CT processes involving molecular states (Figure 9I) and molecular and metallic states (Figure 9II y III). In general, the chemical SERS enhancement factor is considered to contribute enhancement factors on the order of 10-10^3.

2.6.4 Nanoparticle interactions and plasmon coupling. The dimer case

Isolated particles such as single spheres nanoparticles, do not exhibit very large EFs. They are typically on the order of only 10^3-10^6 and are therefore not relevant for single-molecule SERS. In contrast, very high EFs are observed in highly localized regions ("hot-spots") in the junctions between two particles where local field enhancement takes place due to coupling between plasmon resonances.[105] Hot-spots have been claimed to provide extraordinary enhancements of up to 10^{10}-10^{11} orders of magnitude to the SERS signal (proportional to $|E|^4$) in areas of subwavelength localization.[106,107] As a result, hot-spots are critically important for SERS and, if sufficient in density, can dominate the properties of any SERS active substrate within which they reside.

A model for plasmon coupling has already been developed from electrodynamic theory and experimental LSPR spectra of assembled nanostructures. Thus, Norlander and Halas[108,109] established that plasmon coupling can be interpreted in a similarly to molecular hybridization. In this well-known model the plasmon modes of two interacting nanoparticles hybridize either in-phase or out-of-phase to form a lower energy bonding plasmon mode and a higher energy antibonding plasmon mode (Figure 10).[109] The polarization of incident light field along the interparticle axis (longitudinal polarization) leads to an in-phase and out-of-phase combination that reflects a bonding (σ) and an antibonding (σ^*) mode, respectively. Nevertheless, the situation is opposite when the polarization is perpendicular to the interparticle axis (transverse polarization). The in-phase hybridization is an antibonding mode (π^*) and the out-of phase

coupling is a bonding mode (π).[109] Plasmon hybridization allows us to express the fundamental plasmon modes of dimers as linear combinations of the plasmons of individual nanoparticles, in a manner analogous to molecular orbital theory (Figure 10F). Thus, the dipole (l=1) plasmon mode of each individual nanoparticle splits into two distinct collective modes, "bonding" and "antibonding" modes. In the case of a dimer excited by light polarized along its interparticle axis, the lower energy (bonding) mode has mutually aligned longitudinal dipoles that lead to a mode with a large induced dipole and a strong coupling to the far field. This mode, also known as "bright mode", has a main contribution to the optical properties of a plasmonic dimer.

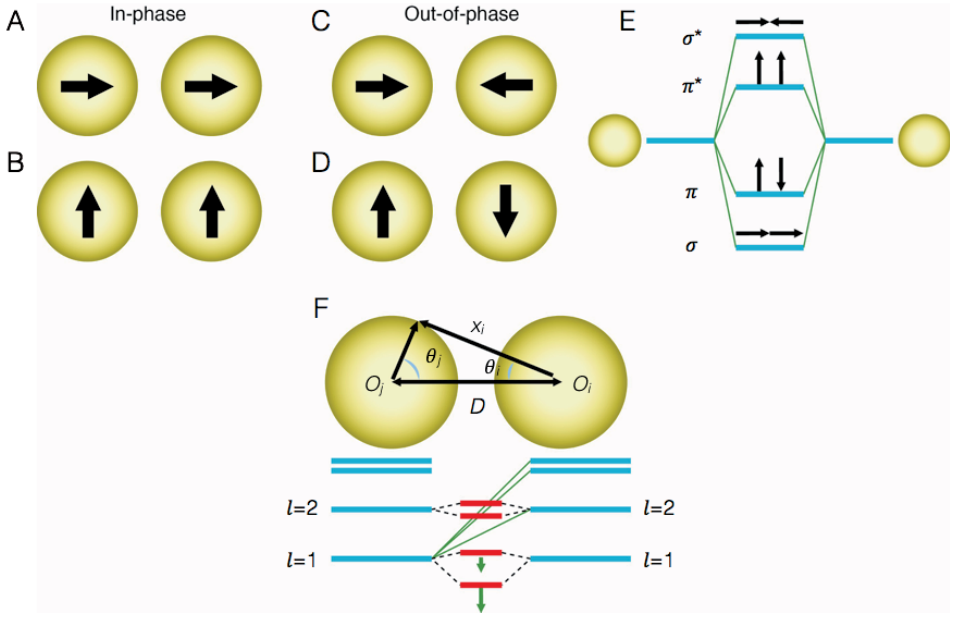

Figure 10. (A) (A-D) Plasmon coupling of two symmetric equivalent particles: in-phase modes for longitudinal (A) and perpendicular (B) polarization and out-of-phase modes for longitudinal (C) and perpendicular (D) polarization. (E) Hybridization model using a coupled dipole-dipole model. (F) Illustration displaying the plasmon hybridization in a nanoparticle dimer. Nanosphere plasmons on the two particles interact and form bonding and antibonding dimer plasmons.

On the other hand, electromagnetic theory predicts that the distance between two particles critically determines the field enhancement in the hot-spot of a dimer. Moreover, some studies have shown that the

electromagnetic enhancement for such a dimer is strongly dependent on the particle size, shape, separation as well as the dielectric properties of the surrounding environment and the metal itself as well as the arrangement with respect to the polarization direction of the incident light.[99,110,111]

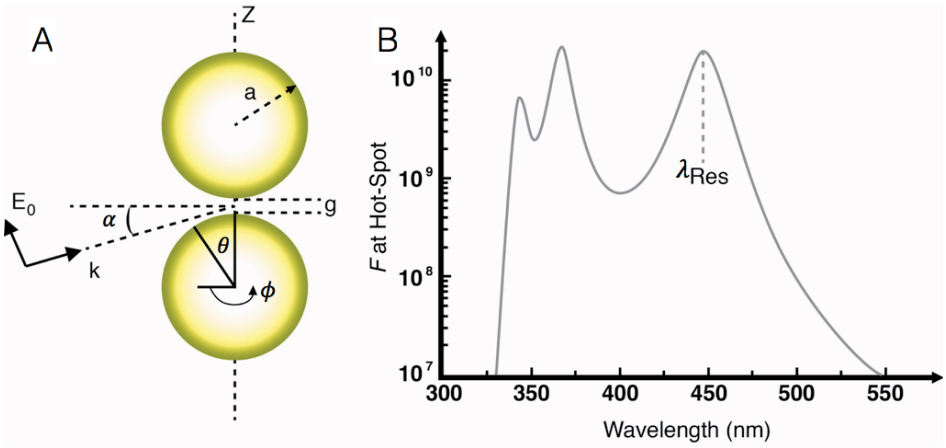

Figure 11. (A) Schematic illustration of simplified dimer geometry formed by two nanospheres of radius a separated by g for electromagnetic calculation. (B) Enhancement factor at the hot-spot formed between two silver 25-nm spheres separated by 2 nm (α = 0). Reproduced from reference[112].

Figure 11A shows, as a schematic, a specific case of a dimer of two silver spheres in air. The polarization of the incident field is aligned along the dimer axis (α = 0). This is the configuration where the largest enhancement is predicted at the hot-spot in the gap between the two particles. Figure 11B shows the wavelength dependence of the enhancement factor at the hot-spot, i.e., at the surface of one of the particles along the dimer axis in the gap. The resonance due to dipolar interaction between the two spheres is the most redshifted and occurs at $\lambda \approx 448$ nm. It would be further redshifted to $\lambda \approx 542$ nm in water and even further if the particles were not spheres. This example only takes into consideration molecules directly adsorbed on the metallic surface and ignore effects of additional layers of molecules. It is generally believed that this first layer contributes to most of the SERS signal.[113]

Besides, hot-spots do not only occur in the gap between two particles, but also at sharp edges and tips;[114,115] the latter is the basis for tip-enhanced Raman scattering (TERS).[116]

2.7 Colloidal nanostructures

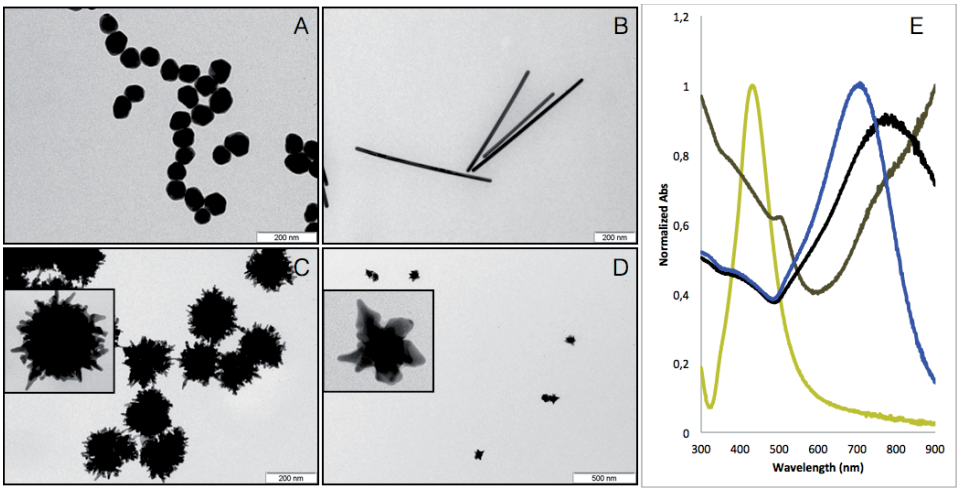

Figure 12. Electron micrographs of some plasmonic nanostructures varying shape and composition (A) silver spheres, (B), gold rods, (C) gold chestnuts and (D) gold stars. (E) Plasmonic response of nanostructures: (yellow line) silver spheres, (blue line) gold stars, (brown line) gold rods and (black line) gold chestnuts.

As already mentioned above, noble metal nanoparticles in suspension, predominantly made of Ag or Au, represent one of the simplest and easiest route to SERS for their versatility and easy synthesis with a high degree of control over the composition, shape and size (Figure 12). These solids consist of hundreds to a few thousand of atoms each and are stabilized by polymers, surfactants, proteins, and aliphatic molecules, among others. Their size usually ranges from 2-3 nm to about 500 nm. In general, it can be stated that silver is a much more efficient optical material than gold, giving rise to SERS signal 10 to 100 fold higher than similar gold nanostructures.[117] First reason to this affirmation is that the scattering contribution is larger in the case of the silver compared to gold. Additionally, silver can be excited from the UV to the IR while gold is restricted to the red or IR owing to damping by the interband transitions.[111]

Plenty of synthetic interest in the field resulted in the development of a high number of methods for the preparation of colloidal nanostructures. The two most popular approaches are the top–down and bottom–up nanofabrication.[118] A typical top down method involves the mechanical grinding of bulk metals and subsequent stabilization of the resulting nanoscaled metal particles by the addition of colloidal protecting agents. On the other hand, the bottom up methods of wet chemical nanoparticle synthesis rely on the chemical reduction of metal salts, electrochemical pathways, or controlled decomposition of metastable organometallic compounds. A large variety of polymers and surfactants are used to control the growth of the primarily formed nanoclusters and to prevent them from aggregating.[119] It is likely that the most popular method for the preparation of a suspension of gold nanospheres colloids in water is the one designed by Turkevich,[76] The Turkevich method comprises the reduction of the precursor gold salt $HAuCl_4$ in a boiling trisodium citrate ($C_6H_5Na_3O_7{\cdot}2H_2O$) solution.[77] $C_6H_5Na_3O_7{\cdot}2H_2O$ provides electrostatic stabilization and also allows for easy surface funcionalization of the as-prepared gold nanoparticles. This method was later extended and modified by a number of authors[120,121] and it is now possible to produce spherical gold particles in water using a wide range of stabilizing molecules with particle sizes ranging from few nanometers up to hundreds of nm. Moreover, many other methods have been devised to produce nanoparticles of different shapes such as monodisperse gold nanorods[122–124]. The synthesis of rod-shaped gold nanoparticles has been carried out by two main routes: the use of rigid templates;[125] and seeded growth in the presence of surfactants, such as cetyl-trimethylammonium bromide (CTAB).[126–128]

Regarding the synthesis of silver nanoparticles, the control over size and shape is much more difficult than in the case of gold due to the higher reactivity of silver. The first chemical methods described for the synthesis of silver NPs in solution are the methods reported by Lee-Meisel[129] and Creighton[130]. The first one is a variation of the Turkevich method,[77] but replacing gold(III) chloride trihydrate ($HAuCl_4$) with silver nitrate ($AgNO_3$). In this method, the silver nanoparticles obtained usually show a wide-ranging size (high polydispersity) and shape (spheres, rods and triangles)

distribution, with a mean particle size around 60 nm. On the other hand, the Creighton method involves the reduction of $AgNO_3$ with sodium borohydride ($NaBH_4$) in an ice-bath. This method provides silver nanoparticles of about 10 nm with a narrow-range size distribution (monodisperse).

On the other hand, the degree of anisotropy has been identified as a major tool for engineering the properties (mechanical, optical, electronic, magnetic, etc.) of nanomaterials, with the additional attractive feature of displaying different properties in different directions. As a consequence, the controlled synthesis of anisotropic nanoparticles is of great importance for application in many fields such as photonics, electronics, sensing, or biomedicine.[53,131] Several synthetic methods related to the production of silver and gold anisotropic nanoparticles have been developed over recent years: the seed-mediated synthesis,[132,133] the polyol synthesis,[134] the biological synthesis,[135] the hydro/solvothermal synthesis,[135] the electrochemical synthesis[136] or template-mediated synthesis.[137] For that reason, the design of particles with sharp tips such as triangles, elongated nanorods, nanowires, or star-shaped (Figure 12B-D) colloids is a key subject in modern nanoscience because of their unique optical properties such as a high sensitivity toward local changes in the dielectric environment or a large electromagnetic field concentration at these sites within the particle.[138]

2.7.1 Nanoparticle stabilization

A stable colloidal solution is one in which the particles resist aggregation. Moreover it exhibits a long shelf life. Particle aggregation refers to formation of assemblages in a suspension and represents a mechanism leading to destabilization of colloidal systems. During this process, particles dispersed in the liquid phase stick to each other, and spontaneously form irregular particle clusters. This will depend upon the balance of the repulsive and attractive forces that exist between particles as they approach one another. If all the particles have a mutual repulsion, then the dispersion will remain stable. However, if the particles have small

or no repulsive forces between them, some instability mechanism will eventually take place producing the aggregation of the system.[139] Once particle aggregates have formed, they will not easily disrupt. In the course of aggregation, the aggregates will grow in size, and may consequently settle to the bottom of the container, which is referred to as sedimentation.

This process of aggregation can occur mainly by two different means, coagulation or flocculation. Coagulation means the formation of compact aggregates that lead to macroscopic separation. Flocculation is the formation of a loose or open network (flocs), which may or may not separate macroscopically. Usually, coagulation is irreversible whereas flocculation can be reversed.

There are two main mechanisms to provide colloidal stability on nanoparticles, *steric stabilization* and *electrostatic stabilization* (Figure 13). In the *steric stabilization mechanism*, layers of large molecules, such as long chain polymers or surfactants, are adsorbed onto the metallic surface of nanoparticles to form a physical barrier that can prevent aggregation and maintain colloidal stability. To understand *electrostatic stabilization* and the processes concerning colloidal stability, the scientists Derjaguin, Landau, Verwey and Overbeek developed a theory (DLVO) in the 1940s, which proposed a mechanism for the stability of colloidal systems comprising double layer repulsion and the van der Waals attractive forces.

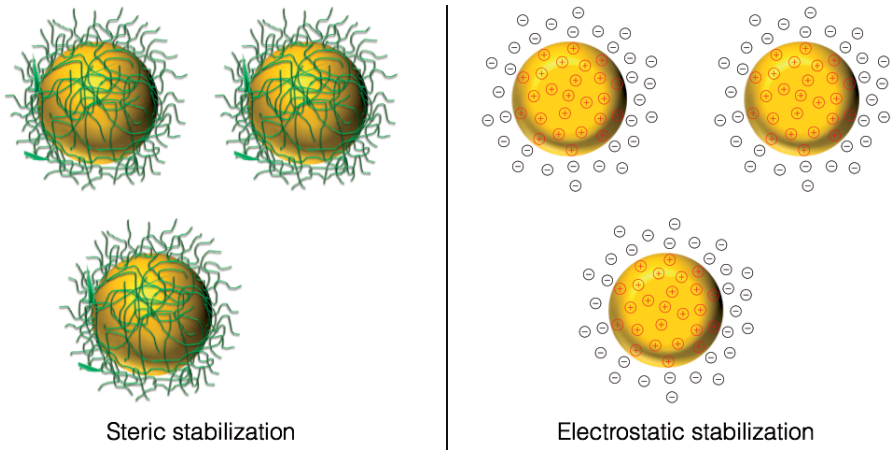

Figure 13. Main types of nanoparticle stabilization.

2.7.1.1 Double layer repulsion

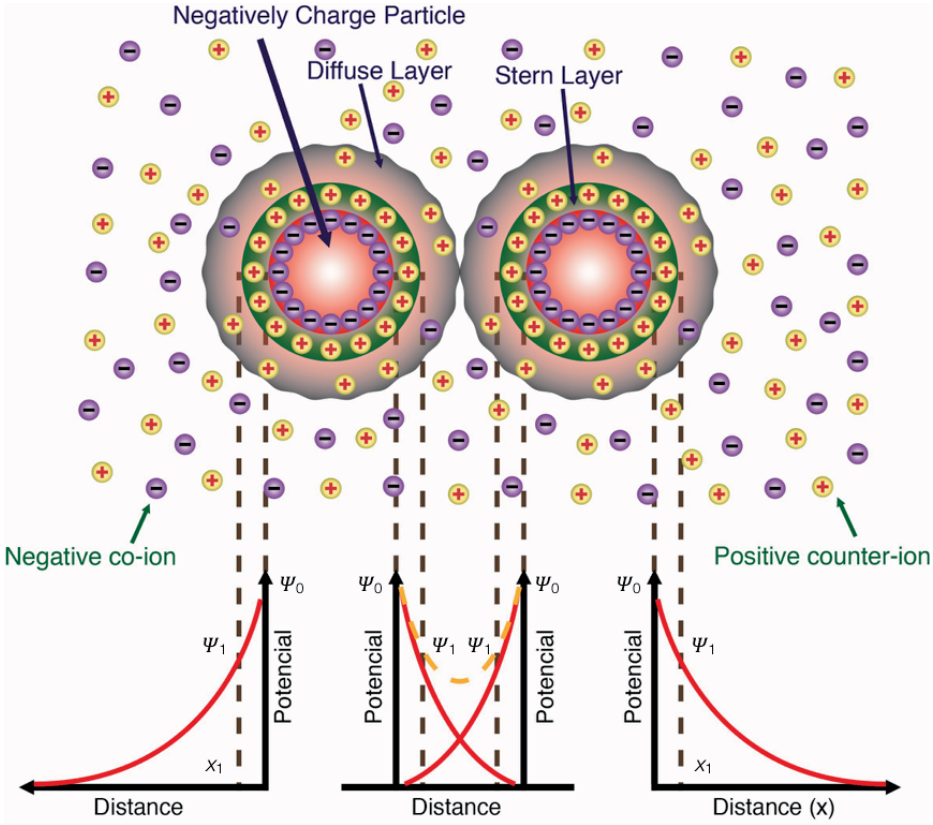

Figure 14. Schematic representation of the electric double layer for two nanoparticles. The distribution of counter-ions and co-ions as a function of the distance to a charged surface and the behavior of the lectectric potential (Ψ), as a function of the distance (x) to the particle surface is shown. Ψ_0 is the potential at the surface of the particle and Ψ_1 the potential at x_1 (commonly known as the zeta potential ζ) the distance from the plane of the counter-ion from the surface.

When a nanoparticle is in an aqueous electrolyte, its surface charge may be determined by four different parameters: solution pH, adsorbed ions or polyelectrolytes, preferential dissolution of lattice ions, and electronic charge. Generally, once the particle surface is charged, the concentrations of both counter-ions and co-ions are distributed within a certain region close to the surface. This region, known as the electrical double layer and shown in Figure 14, was first discussed and modeled by Helmholtz in 1879. It was later modified by Gouy and Chapman in 1913, and again modified

by Stern,[140] to describe the distribution of counter-ions and co-ions and the behavior of electric potential (Ψ), as a function of distance (x) from the particle surface.

The electrical double layer consists of two regions, the inner compact layer (Stern layer) and the diffuse layer. The Stern plane comprises, in the case of a positively charged surface, strongly polarized water molecules and desolvated ions, both of them are chemisorbed onto the surface. The Stern layer is usually about 0.5 nm thick. The diffuse layer consists of hydrated, negative counter-ions, which are present and effectively neutralize the positive ions at the particle surface. The actual distribution of ions within the vicinity of the charged surface is determined by the electric field emanating from the particle surface, and by Brownian motion. According to the Boltzmann distribution, the number density ($n\pm$), of each ionic species per unit volume at a given electric potential (Ψ) can be determined by the expression:

$$n_{\pm} = {n_{\pm}}^{0} e^{\frac{-z_{\pm} e\Psi}{kT}}$$

Equation 24

where ${n_{\pm}}^{0}$ is the corresponding bulk concentration of each ionic species, e the electron charge, k the Boltzmann constant and T the absolute temperature. The net density of charge, ρ, per unit volume at Ψ is given by:

$$\rho = -2|z|en^{0} sinh\left(\frac{|z|e\Psi}{kT}\right)$$

Equation 25

where $|z|$ is the absolute electrolyte valence. ρ and Ψ are related through the Poisson equation:

$$\nabla^{2}\Psi = -\frac{\rho}{\varepsilon_{r}\varepsilon_{0}}$$

Equation 26

ε_0 being the permittivity of vacuum and ε_r the relative permittivity of the medium in the diffuse layer. Combining Equation 25 and Equation 26 yields:

$$\nabla^2\Psi = \frac{-2n^0|z|e}{\varepsilon_r\varepsilon_0} sinh\left(\frac{|z|e\Psi}{2kT}\right)$$

Equation 27

with the appropiate boundary conditions ($\Psi = \Psi_0$ when $x = 0$ and $\Psi = 0$, $\frac{\partial\Psi}{\partial x} = 0$ when $x = \infty$), assuming low potentials, i.e. $\left(\frac{|z|e\Psi}{2kT}\right) \ll$, (i.e. Debye-Hückel approximation), the solution of Equation 27 can be written as:

$$\Psi = \Psi_0 e^{-kx} \text{ (for a flat-plate surface where } ka \ll 1)$$

Equation 28

$$\text{being } k = \left(\frac{2F^2cz^2}{\varepsilon_r\varepsilon_0 RT}\right)^{1/2}$$

Equation 29

with Ψ_0 the surface potential of the plate and the remaining symbols having their usual meanings. Through Equation 29, the double layer thickness k^{-1} in the diffuse regime is said to undergo compression with increasing electrolyte concentration. As can be seen in Fig x.x, the potential changes linearly from Ψ_0 to Ψ_1 in the Stern regime ($0 < x < x_1$), with Ψ varying exponentially with distance x from the surface in the diffuse double layer, according to Equation 28 Once again, the Boltzmann distribution predicts that Ψ_0 depends on $\varepsilon_r\varepsilon_0$, the surface charge density σ_0, and k according to the expression:

$$\sigma_0 = \varepsilon_r\varepsilon_0 k\Psi_0$$

Equation 30

Consequently, the potential at x_1 is reduced to

$$\Psi_1 = \Psi_0 - \frac{\sigma_0 x_1}{\varepsilon_1\varepsilon_0}$$

Equation 31

with being ε_1 the relative permittivity in the Stern region. Ψ_1 is usually regarded as being numerically close to the exponentially determined zeta potential, denoted by the symbol ζ. When the same conditions and procedures as for Equation 28 for a flat-plate surface are applied, the potential for a spherical particle of radius *a*, at distance *r* from the center of the sphere, can be written as:

$$\Psi = \Psi_0 \frac{a}{r} e^{-k(r-a)}$$

Equation 32

When two equal, spherical particles of radius *a* approach each other at a surface-to-surface interparticle separation *D*, their electrical double layers of like sign overlap with each another and, assuming a constant surface potential and $ka \gg 1$, they experience a repulsive interaction energy (V_R):

$$V_R = 2\pi\varepsilon_0\varepsilon_r a{\Psi_0}^2 ln(1 + e^{-kD})$$

Equation 33

Equation 33 is applicable for large particles and low electrical double layer overlap whereby the particles are not too close to each other. For a small electrical double-layer overlap (low surface potentials) and $ka \gg 1$, i.e. double-layer of nanosized spherical particles, then Equation 33 is reduced to:

$$V_R = 2\pi\varepsilon_0\varepsilon_r a{\Psi_0}^2 (e^{-kD})$$

Equation 34

This is the most appropriate equation for nanosized particles.

2.7.1.2 The van der Waals Forces

The attractive van der Waals forces, comprising the dispersion and London forces are responsible for attraction between any types of atoms and molecules whether charged or neutral, and are also present in the interaction between particles in any suspension medium. The interaction

energy acting between the two atoms varies inversely proportional to the sixth power of their distance of separation *D*:

$$V_A = -\frac{C}{D^6}$$

Equation 35

where *C* is the London constant, the coefficient in the atom-atom pair potential. The same dipole-dipole interaction between neutral atoms or molecules is also present in the interaction between colloidal particles. The interaction energy between two particles is calculated by summing up all the attractive interactions between molecules of one particle of volume V_1 with molecules of another particle of volume V_2:

$$V_A = -\iint \frac{\rho_1 \rho_2 C_{12}}{D^6} dV_1 dV_2$$

Equation 36

where ρ_1 and ρ_2 are the numbers of molecules per unit volume in particles 1 and 2 respectively, and C_{12} is the London Constant. If the colloid particles *in vacuo* are regarded as two infinitely large flat plates of the same material, then the integration of Equation 36 yields an interaction energy per unit area:

$$V_A = -\frac{A}{12\pi D^2}$$

Equation 37

with the Hamaker constant $A = \pi^2 \rho^2 C$. The integration in Equation 36 has been applied to other geometries. In the case of two, identical spherical particles of radii *a*, the expression for V_A takes the form:

$$V_A = -\frac{A}{12}\left[\frac{1}{y(y+2)} + \frac{1}{(y+1)^2} + 2ln\left(\frac{y(y+2)}{(y+1)^2}\right)\right]$$

Equation 38

where $y = \frac{D}{2a}$ for $a \ll D$, Equation 38 then reduces to:

$$V_A = -\frac{Aa}{12D}$$

Equation 39

2.7.1.3 Total Potential Energy of Interaction

Derjagin and Landau[141] and Verwey and Overbeek[142] independently developed a theory (DLVO theory) to calculate the energy (V_T) of interaction between spherical particles as a function of interparticle separation and other parameters. V_T is considered to be the sum of the electrostatic repulsion V_R and van der Waals attraction V_A. For small, nanosized particles this gives:

$$V_T = 2\pi\varepsilon_0\varepsilon_r a\Psi_0{}^2(e^{-kD}) - \frac{Aa}{12D}$$

Equation 40

This equation is strictly valid only for $ka \ll 1$ and for small double layer interactions. The electrical double layer repulsive energy decays exponentially with the distance, while the attractive interaction decreases with the inverse power of interparticle separation. Consequently, the van der Waals attraction will predominate at both small and large interparticle distances, while the double layer repulsion may predominate at intermediate distances, depending on solution conditions.

Particle stability depends on the primary maximum energy relative to the thermal energy. If the primary maximum is much larger than the thermal energy, then the particles should be stable. Otherwise, the particles can overcome the barrier. Once within this distance, the van der Waals forces pull the particles into the deep primary minimum that leads to irreversible coagulation. The secondary minimum, which may be present in some systems, is a regime where particles become weakly flocculated but they can be easily redispersed by physical agitation, for example, by stirring or sonication.

2.8 Biomedical applications and SERS sensing

SERS is a powerful and reliable analytical technique that has already proven to be particularly effective for diagnosis and biomedical applications.[21,22] SERS combines the high level of molecular structural information of a vibrational spectroscopy with ultrasensitive detection limits. This allows to detect molecules and to establish their structural identity in very small quantities down to the single-molecule level. In serious medical issues the fast and accurate detection of pathogens is literally a matter of life and death. Therefore, SERS biosensors can be applied in the detection of biological samples and diseases. These include various types of cancer,[143] infections,[144] and prionic diseases such as Alzheimer and Parkinson.[145]

We saw in sections 2.6.1 and 2.7 that recent spectacular advances in nanofabrication techniques fueled the development of a large variety of rationally designed SERS substrates with an optimized, uniform and reproducible response. This successfully translated the spectacular analytical potential of SERS to widely accepted and commercially viable sensing applications. The dependence of LSPRs with parameters such as size, shape, composition and surrounding medium provides multiple possibilities for tuning the optical response and, thus, optimizing the SERS performance of the plasmonic nanostructure for a specific application. In conjunction with the control of the signal amplification provided by the optical enhancer, a key step in the practical implementation in sensing applications (including SERS) is the appropriate chemical functionalization of the "bare" metallic surface. Two design approaches are commonly used to devise plasmonic nanostructures as SERS sensing platforms: *direct SERS* and *SERS tags*.

Direct SERS is achieved by directly acquiring the SERS spectrum of the analyte upon its chemisorption on the plasmonic surface. Direct sensing is adequate for multiplex analysis which allows for simultaneous measurements of various target analytes in a single cycle of the assay within the same sample where the particle itself is the sensing element.

Multiplex analysis can also be applied for indirect detection, where the particles are surface functionalized with one or more ligands with the ability to react selectively at the existence of certain substances or encoded particles, that act as cellular or molecular labels.[146] Direct sensing provides a flexible platform and can lead to ultrasensitive detection. However, a number of other species beside the target molecules can be detected simultaneously when performing *direct SERS* thus hampering the application of this strategy when complex analytical matrixes like those in bio- or environmental applications are involved. In fact, the overlapping of vibrational modes of different molecules is very likely when the number of targets and background species is high. This makes interpretation of the overall vibrational spectrum extremely difficult or nearly impossible.

On the other hand, *SERS tags* can be prepared by using an efficient plasmonic substrate which is labelled with a SERS molecule, protected with an external inert layer and functionalized with the appropriate selective chemoreceptor (such as an antibody, or aptamer). In this case, the identification and quantification of the analyte are indirectly correlated to the presence and intensity of the specific SERS label. For this reason, *SERS* tags have a considerable potential for ultrasensitive detection of biomolecules such as hemoglobin, glucose, cancer genes, pathogens, biological toxins and viruses.

3 Objectives

As previously stated on the introduction, the aim of this thesis is the development of a reliable sensor for the multiplex detection and quantification of microorganisms in biological samples for PJI diagnosis. This sensor device is based on plasmonic NPs, microfluidics, and SERS spectroscopy. Therefore, the research should be performed following the logical progression indicated below:

1- One of the key concepts for the design of this bioanalytical device consists in the development of effective SERS-encoded plasmonic nanostructures. Such nanostructures need to fulfill several requirements: (1) provide high SERS efficiency with a huge number of different Raman reporters (characterized by its unique spectroscopic fingerprint and high Raman cross-section), (2) be colloidally stable in an aqueous environment of high salt concentration, and (3) their surface chemistry should allow its biofuncionalization with antibodies or aptamers. To achieve these requirements, a synthetic protocol based on molecules that provide steric and electrostatic nanoparticle stabilization during the codification process, such as 11-mercaptoundecanoic acid, should be developed. Moreover, nanoparticles with different shapes and composition has to be produced in order to evaluate their optical properties.

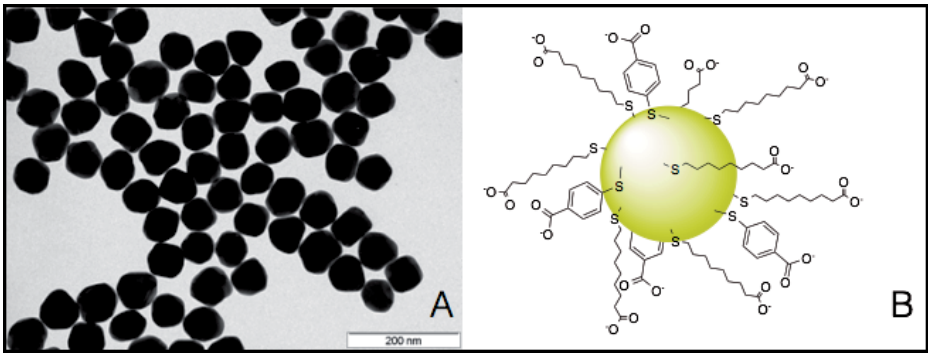

Figure 15. (A) Representative TEM image of sodium citrate stabilized silver nanospheres. (B) Schematic representation of a silver nanosphere stabilized with 11-mercaptoundecanoic acid and encoded with 4-mercaptobenzoic acid.

2- Once NPs were encoded successfully, they have to be funcionalized with particular antibodies yielding final SERS-tags. Antibodies are large proteins that have specific affinity for pathogens such as bacteria and viruses. Therefore, nanoparticle bioconjugation protocols, such as carbodiimde synthetic methods, should be optimized in order to control the number of antibodies per particle.

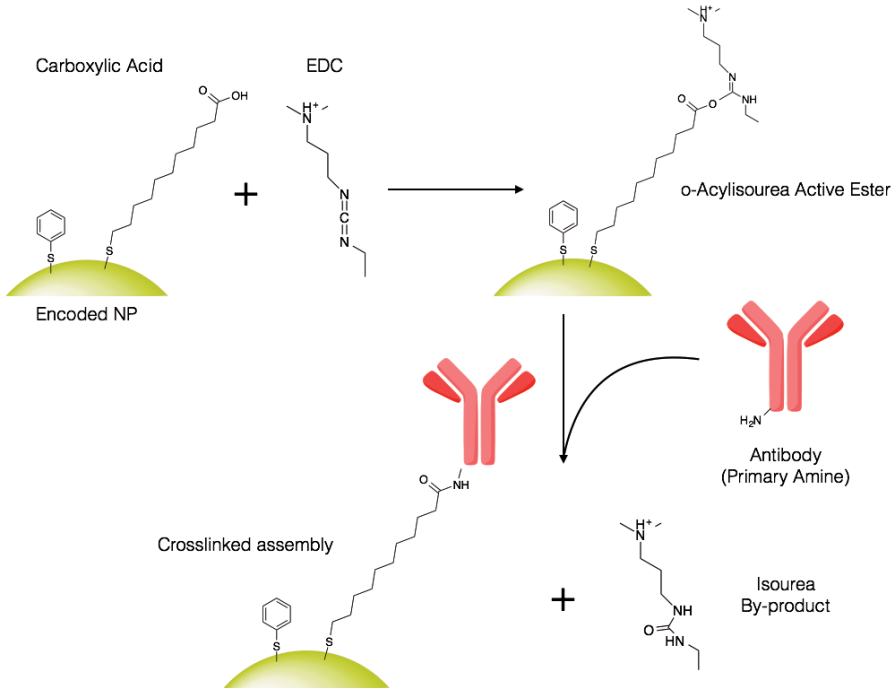

Figure 16. EDC (carbodiimide) crosslinking reaction scheme. This Carboxyl-to-amine crosslinking reaction can be done with peptides, proteins or any chemicals that have respective carboxylate and primary amine groups.

3- In a typical suspension assay, a mixture of different SERS-tags (each of them carrying a unique Raman reporter and bioreceptor) will be added to the fluid of interest in a microfluidic system. The NPs should produce a relatively weak Raman signal when they are dispersed in a fluid. In contrast, the presence of one of the targeted pathogens should triggers the accumulation of its partner NPs on the antigen-carrying membrane of the microorganism rapidly reaching full random coverage.[147] In that case, Raman scattering should be enhanced by several orders of magnitude allowing for single microorganism detection. For that reason, a preliminary

study of the optical properties of different encoded NPs assembled on bacteria proxies (i.e., 3 μm silica or polystyrene beads) should be necessary to find the more suitable encoded nanostructure.

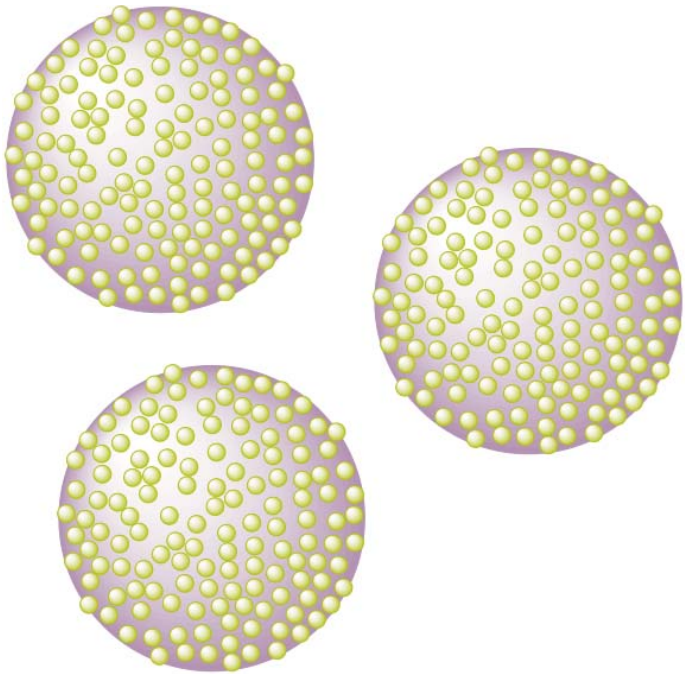

Figure 17. Schematic representation of a polystyrene or silica beads coated with encoded Ag NPs and used as a bacteria model.

4- The major goal of this technology is an accurate diagnosis in a very short time as compared with all other currently available methods. To this end, bacteria identification and quantification should be tested passing a real sample (previously mixed with the correspondent SERS-tags) through a millifluidic channel where a backscattered detecting laser (785 nm) continuously monitors the liquid stream. The device has to simultaneously quantify multiple different types of bacteria at a rate of minutes per mL of body fluid. The SERS signal of the accumulated NPs on the microorganism membrane should be sufficient enough for this multiplex quantification and not to interfere with the background signal. Moreover, different types of biological fluids (blood, serum, etc.) should be tested to be sure that SERS-tags do not have unspecific interactions with other chemoreceptors present in the sample.

5- Finally, antibodies are an excellent option for the accurate recognition of specific targets but they are very expensive to produce, delicate to handle, and large in size. To solve this problem and as an alternative, encoded nanoparticles could be funcionalized with a family of biomolecules with the same specificity or even larger (i.e. aptamers) that can be produced synthetically without batch-to-batch variability, are more robust (i.e. less affected to denaturalization by exogenous factors as temperature changes) and have a shorter size (may yield many efficient hot-spots).